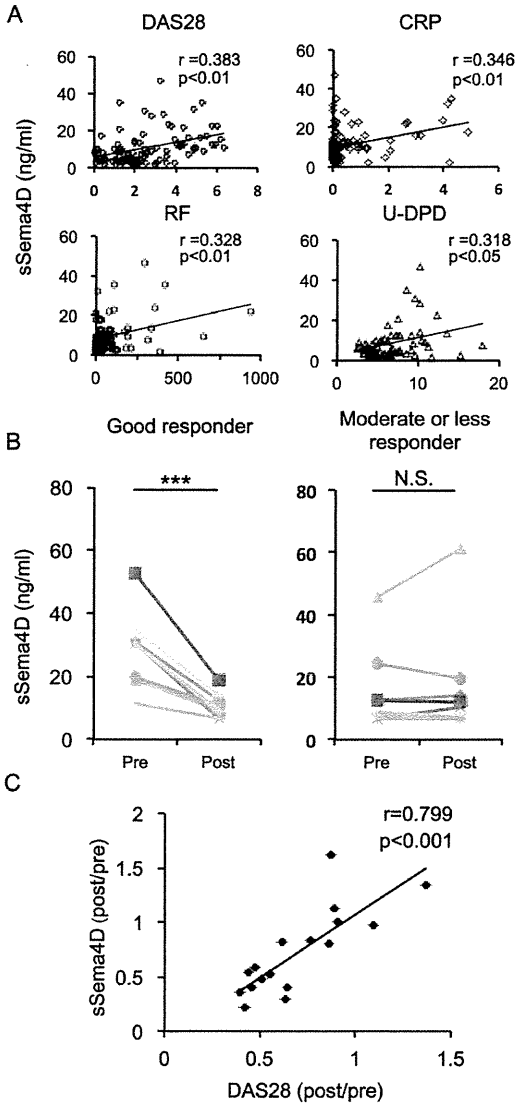

Figure 2. Correlations of serum levels of soluble Sema4D with RA disease activities.
A) Serum levels of sSema4D were positively correlated with disease activity score 28 (DAS28), C reactive protein (CRP), urinary deoxypyridinoline (u-DPD), and rheumatoid factor (RF). B) Serum sSema4D levels before and after bDMARDs treatment in nine good responders and eight moderate responders or non-responders, according to the DAS improvement criteria. C) Correlation of serum sSema4D reduction (post-biologics/pre-biologics) with DAS28 improvement (post-biologics/pre-biologics) n = 17. * $p < 0.05$, ** $p < 0.01$, *** $p < 0.001$.

118x235mm (150 x 150 DPI)

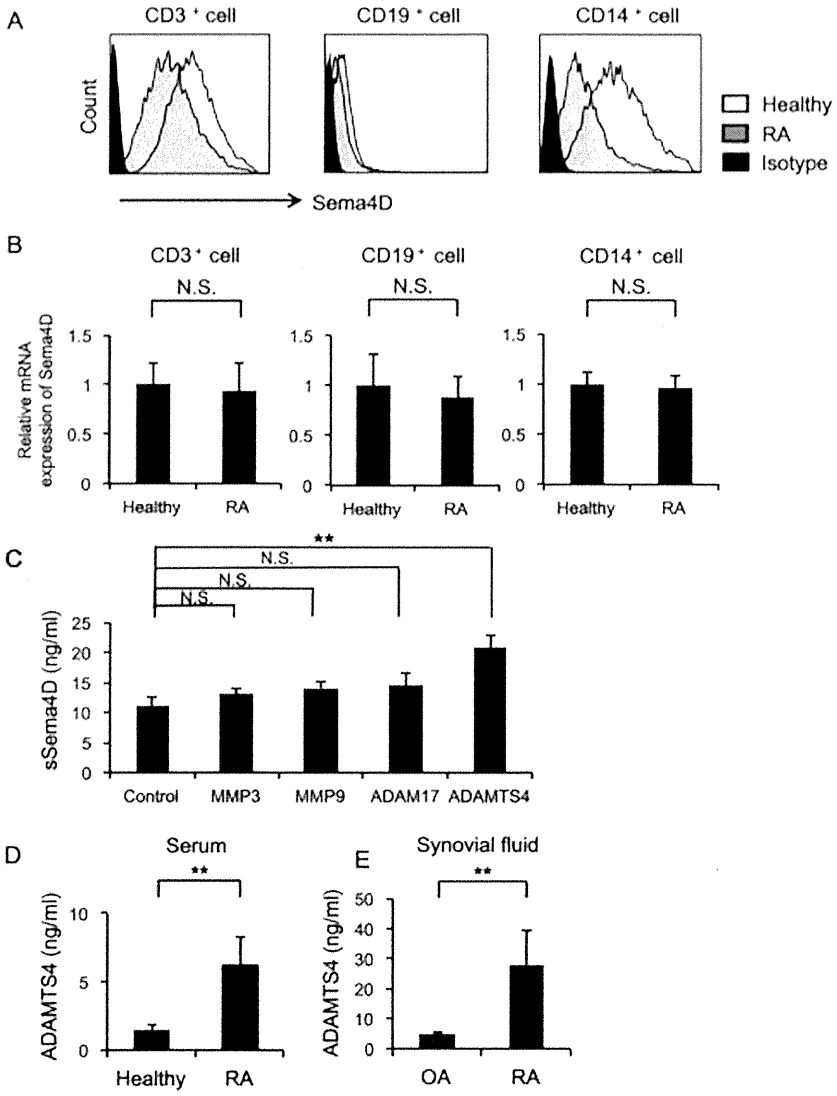

Figure 3. Sema4D expression, and soluble Sema4D production with ADAMTS4 as the sheddase. A) Histogram of cell-surface expression of Sema4D in peripheral blood in CD3+, CD19+, and CD14+ cells. Results shown are representative findings from five RA patients and five healthy individuals. B) mRNA expression of Sema4D in peripheral blood CD3+, CD19+, and CD14+ cells. Results from five RA patients and five healthy individuals were shown. C) Levels of sSema4D in culture supernatant of THP-1 cells cultured with recombinant MMP3, MMP9, ADAM17, and ADAMTS4 (n = 5 per group). Representative results of three independent experiments are shown. D) Serum levels of ADAMTS4 in 20 RA patients and 16 healthy individuals. E) Synovial fluid levels of ADAMTS4 in seven RA patients and ten OA patients. * $p < 0.05$, ** $p < 0.01$, *** $p < 0.001$.

178x228mm (72 x 72 DPI)

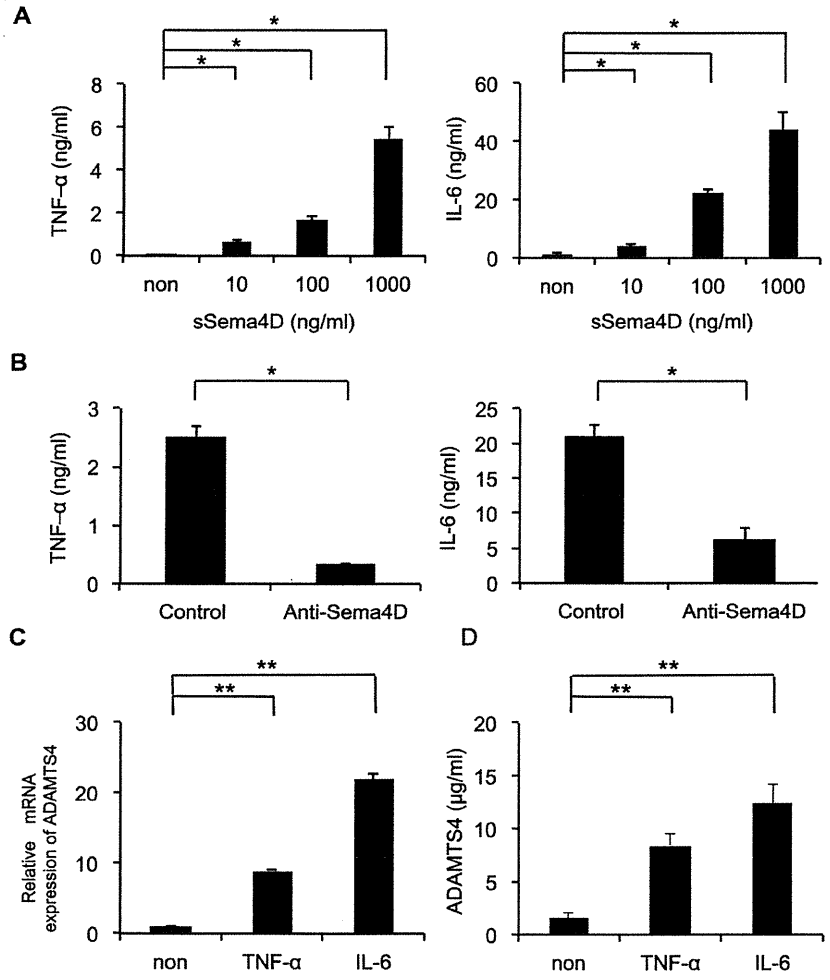

Figure 4. Inflammatory cytokine production induced by Sema4D, and elevated ADAMTS4 expression by inflammatory cytokines

A) TNF-α and IL-6 levels in culture supernatant of CD14+ monocytes from RA patients stimulated with naturally cleaved sSema4D for 72 hours. Representative results of three independent experiments are shown. B) TNF-α and IL-6 levels in culture supernatant of CD14+ monocytes from RA patients stimulated with naturally cleaved sSema4D for 48 hours, with or without anti-Sema4D antibody. Representative results of three independent experiments are shown. C, D) Elevated ADAMTS4 mRNA and protein levels in primary cultures of synovial cells from RA patients. Data were compiled from five independent experiments. * $p < 0.05$, ** $p < 0.01$, *** $p < 0.001$.

191x214mm (150 x 150 DPI)

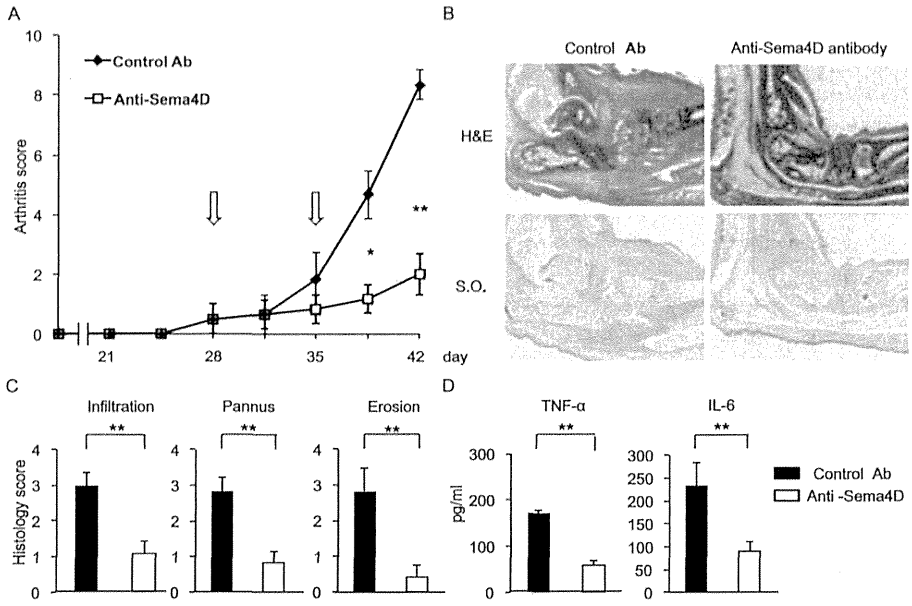

Figure 5. Blocking Sema4D ameliorates the severity of collagen-induced arthritis (CIA) in mice. A) Average arthritis scores of CIA mice. Anti-Sema4D or control antibody (50 mg/kg) was administrated intraperitoneally on days 28 and 35 (arrow) (n = 6 per group). Data are representative of three independent experiments. B) Sections of a mouse ankle joint on day 42 after first immunization. Sections were stained with H&E and Safranin O. C) Average pathological scores of paw sections on day 42 (n = 12 per group). D) Serum levels of IL-6 and TNF-α on day 42 (n = 6). Data are means ± SEM, and are representative of three independent experiments. * $p < 0.05$, ** $p < 0.01$, *** $p < 0.001$.

254x171mm (150 x 150 DPI)

OPEN ACCESS Freely available online

PLOS | ONE

Estrogen-Dependent Proteolytic Cleavage of Semaphorin 4D and Plexin-B1 Enhances Semaphorin 4D-Induced Apoptosis during Postnatal Vaginal Remodeling in Pubescent Mice

Takuji Ito[1☯], Tao Bai[2☯], Tetsuji Tanaka[2☯], Kenji Yoshida[1], Takashi Ueyama[3], Masayasu Miyajima[4], Takayuki Negishi[1], Takahiko Kawasaki[5], Hyota Takamatsu[6], Hitoshi Kikutani[7], Atsushi Kumanogoh[6], Kazunori Yukawa[1]*

1 Department of Physiology, Faculty of Pharmacy, Meijo University, Nagoya, Japan, **2** Department of Obstetrics and Gynecology, Wakayama Medical University, Wakayama, Japan, **3** Department of Anatomy and Cell Biology, Wakayama Medical University, Wakayama, Japan, **4** Laboratory Animal Center, Wakayama Medical University, Wakayama, Japan, **5** Division of Brain Function, National Institute of Genetics, Graduate University for Advanced Studies (Sokendai), Mishima, Japan, **6** Department of Immunopathology, Research Institute for Microbial Diseases, Osaka University, Suita, Japan, **7** Department of Molecular Immunology, Research Institute for Microbial Diseases, Osaka University, Suita, Japan

Abstract

Around the fifth week after birth, the vaginal cavity in female mouse pups opens to the overlaying skin. This postnatal tissue remodeling of the genital tract occurs during puberty, and it largely depends upon hormonally induced apoptosis that mainly occurs in the epithelium at the lower part of the mouse vaginal cavity. Previously, we showed that most BALB/c mice lacking the class IV Semaphorin (Sema4D) develop imperforate vagina and hydrometrocolpos; therefore, we reasoned that the absence of Sema4D-induced apoptosis in vaginal epithelial cells may cause the imperforate vagina. Sema4D signals via the Plexin-B1 receptor; nevertheless detailed mechanisms mediating this hormonally triggered apoptosis are not fully documented. To investigate the estrogen-dependent control of Sema4D signaling during the apoptosis responsible for mouse vaginal opening, we examined structural and functional modulation of Sema4D, Plexin-B1, and signaling molecules by analyzing both wild-type and Sema4D−/− mice with or without ovariectomy. Both the release of soluble Sema4D and the conversion of Plexin-B1 by proteolytic processing in vaginal tissue peaked 5 weeks after birth of wild-type BALB/c mice at the time of vaginal opening. Estrogen supplementation of ovariectomized wild-type mice revealed that both the release of soluble Sema4D and the conversion of Plexin-B1 into an active form were estrogen-dependent and concordant with apoptosis. Estrogen supplementation of ovariectomized Sema4D−/− mice did not induce massive vaginal apoptosis in 5-week-old mice; therefore, Sema4D may be an essential apoptosis-inducing ligand that acts downstream of estrogen action in vaginal epithelium during this postnatal tissue remodeling. Analysis of ovariectomized mice also indicated that Sema4D contributed to estrogen-dependent dephosphorylation of Akt and ERK at the time of vaginal opening. Based on our results, we propose that apoptosis in vaginal epithelium during postnatal vaginal opening is induced by enhanced Sema4D signaling that is caused by estrogen-dependent structural changes of Sema4D and Plexin-B1.

Citation: Ito T, Bai T, Tanaka T, Yoshida K, Ueyama T, et al. (2014) Estrogen-Dependent Proteolytic Cleavage of Semaphorin 4D and Plexin-B1 Enhances Semaphorin 4D-Induced Apoptosis during Postnatal Vaginal Remodeling in Pubescent Mice. PLoS ONE 9(5): e97909. doi:10.1371/journal.pone.0097909

Editor: Hiroyasu Nakano, Toho University School of Medicine, Japan

Received January 30, 2014; **Accepted** April 25, 2014; **Published** May 19, 2014

Funding: This work was primarily supported by Grants-in-Aid for Scientific Research from the Ministry of Education, Science, Sports and Culture, Japan (#19590178, http://www.jsps.go.jp/j-grantsinaid/index.html), and partly supported by several grants from the Research Institute of Meijo University. The funders had no role in study design, data collection and analysis, decision to publish, or preparation of the manuscript.

Competing Interests: The authors have declared that no competing interests exist.

* E-mail: kyukawa@meijo-u.ac.jp

☯ These authors contributed equally to this work.

Introduction

In mice, the blind ending of the vaginal cavity in each female pup opens to the skin around 5 weeks after birth when sex hormone level rises in the internal environment; vaginal opening is one of very few postnatal tissue remodeling events in mice [1]. The study of transgenic mice that overexpress the human anti-apoptotic protein Bcl-2 in the vaginal mucosa clearly shows that this postnatal tissue remodeling process depends heavily on massive mucosal apoptosis; these cell deaths occur in a very limited time window and only at the lower distal end of mouse vaginal cavity in the vicinity of skin [1]. Subsequently, several studies involving various types of knockout mice revealed the crucial involvement of proapoptotic Bcl2 family proteins [2,3], along with other signaling molecules, in mouse vaginal remodeling [4,5]. However, the exact mechanisms by which rapid increases of estrogen level in the mouse internal environment induce the extensive apoptosis in vaginal epithelium at the time of puberty remain unknown [1,6]. We found that mice lacking Semaphorin 4D (Sema4D) often develop imperforate vagina and hydrometro-

colpos [7]; Sema4D is a semaphorin that controls axon guidance during neuronal development [8,9].

Semaphorins are a family of secreted and transmembrane glycoproteins with phylogenetically conserved domains; they were originally identified as repulsive axon guidance molecules that function during development of the nervous system [10]. Sema4D (also called CD100) is a class 4 transmembrane-type semaphorin that binds to Plexin-B1, which is a transmembrane receptor and a member of the plexin family, to induce repulsive cytoskeletal changes in growth cones of cultured neurons [11]. Sema4D and Plexin-B1 interact via their conserved sema domains of ~400 amino acids each; each sema domain forms a seven-blade β-propeller fold in the extracellular domain of the respective protein [10,12,13]. Binding of Sema4D to Plexin-B1 causes Plexin-B1 molecules to cluster; this clustering facilitates GTPase activating protein (GAP) activities of the two GAP domains in the intracellular region of each Plexin-B1 molecule [14]. The augmented Plexin-B1 GAP activities in neurons 1) downregulate activities of Ras family members and 2) induce dephosphorylation of Akt and ERK and activation of glycogen synthase kinase (GSK)-3β; these events reduce integrin-mediated cell adhesion to the extracellular matrix, and consequently induce morphological remodeling of growth cones and dendrites in cultured neurons [14,15,16]. In contrast, Sema4D binding to Plexin-B1 on endothelial cells stimulates the activation of the phosphatidylinositol 3-kinase (PI3K)-Akt pathway and of ERK to induce endothelial cell migration [17,18]. Thus the Sema4D signal either facilitates or weakens the same intracellular signaling pathway depending upon the cell type and cellular context. Membrane-bound Sema4D on T lymphocytes is cleaved via metalloprotease-dependent proteolysis, and the extracellular domain is then shed as diffusible secreted protein from a membrane surface to the surrounding extracellular environment [19]. Soluble secreted Sema4D is thought to function as a guidance cue that acts across long distances to inhibit immune cell migration [19]. Plexin-B1 is also converted from a precursor into an active heterodimeric form composed of distinct subunits resulting from proprotein convertase-mediated processing of Plexin-B1 [20]. The proteolytically processed, active form of Plexin-B1 transmits a more intense Sema4D-dependent intracellular signal than does the unprocessed precursor [20].

The high frequency of vaginal atresia and the significant attenuation of vaginal epithelial apoptosis in Sema4D-deficient (Sema4D−/−) mice indicates that vaginal mucosal apoptosis and the vaginal opening process do not occur normally in these mice. Furthermore, we demonstrated that Sema4D binds to Plexin-B1 receptor to induce apoptosis of vaginal epithelial cells in culture. β-Estradiol administration in infant Sema4D-deficient mice does not induce precocious vaginal opening; therefore, Sema4D may function downstream of estrogen action during postnatal vaginal tissue remodeling [7]. However, mouse vaginal opening occurs 5 weeks after birth when estrogen levels increase rapidly in female mice, and the pro-apoptotic signals in the maturing vaginal epithelial cells may be enhanced via estrogen-mediated functional modulation of Sema4D and Plexin-B1. Here, we examined whether estrogen induces structural and functional changes in Sema4D and Plexin-B1 that lead to the induction of vaginal epithelial apoptosis and the consequent tissue remodeling. The results of our study indicated 1) that Sema4D cleavage and Plexin-B1 activation were both estrogen dependent and 2) that these events led to vaginal epithelial apoptosis in this postnatal tissue remodeling event.

Materials and Methods

Generation of Sema4D−/− Mice

Sema4D−/− mice generated by gene targeting [21] were backcrossed with BALB/c mice for 10 generations. Pairs of resultant heterozygous mice were bred to obtain homozygous, knockout mice and their wild-type (WT) littermates. The mice were bred for the preparatory and pairwise in the animal facilities of Wakayama Medical University and the animal center in the Faculty of Pharmacy, Meijo University. Each researcher and each laboratory technician followed the guidelines promulgated by the Physiological Society of Japan and the respective guidelines on animal experiments from Wakayama Medical University and from Meijo University when caring for or sacrificing mice and when conducting protocols involving mice. Each institutional Animal Ethics Review committee, the Wakayama Medical University committee and the Meijo University committee, approved the experimental protocols (approval number: 267; Wakayama Medical University, 2012-yaku-jitsu-8; Meijo University).

Genotype Analysis

Mouse tail DNA, Sema4D gene-specific primers, and PCR were used as described previously to determine each mouse genotype [21].

Immunohistochemistry and TUNEL Assay

Mice were sacrificed by intraperitoneal injection of pentobarbital sodium (Kyoritsuseiyaku Co., Tokyo, Japan) and then subjected to transcardiac perfusion of 4% paraformaldehyde. Each vagina excised from a mouse was fixed overnight in 4% paraformaldehyde solution. Each vagina was then embedded longitudinally in paraffin and cut into 4-μm serial sections. Sections were immunolabeled with anti-cleaved caspase-3 (Cell Signaling Technology, Beverly, MA), anti-Akt (Cell Signaling Technology), or anti-Erk1/2 antibody (Cell Signaling Technology). TUNEL assays were performed basically as described previously [22], using a fluorometric TUNEL assay system (Promega, Madison, WI) following the manufacturer's protocols.

Western Blot

To reduce the variance among samples, dissection of each mouse vagina was conducted as follows. A mouse was sacrificed via intraperitoneal injection of pentobarbital sodium; a laparotomy was then performed to expose the reproductive organs, and the fatty tissues around the vagina were then removed. The pubic bone was resected to view the lower region of the vagina; the urinary bladder, urethra, and rectum were then separated from the vagina. In each case of an unopened vagina, the border area between the lowest end of the vagina and the skin surface of the expected vaginal orifice was transversely cut so that the septum covering the lower extremity of the vagina [1] was included in the vaginal tissue sample; simultaneously, the uterine cervix was pulled ventrally with forceps. In each case of an opened vagina, the region between the vaginal orifice and the surrounding skin was cut while the uterine cervix was pulled ventrally with forceps. Each vagina was obtained via a transverse cut beneath the lowest extremity of the uterine cervix to exclude the cervix; each such vagina was rapidly minced into small pieces on ice. Tissue extracts were prepared by homogenizing the mouse vaginal tissue in T-PER Tissue Protein Extraction Reagent (Thermo Scientific Inc., Waltham, MA) with a protease inhibitor, α-complete (Roche Applied Science, Penzberg, Germany), and a phosphatase inhibitor, PhosStop (Roche Applied Science). The Bio-Rad Protein assay (Bio-Rad, Hercules, CA) was used to measure the

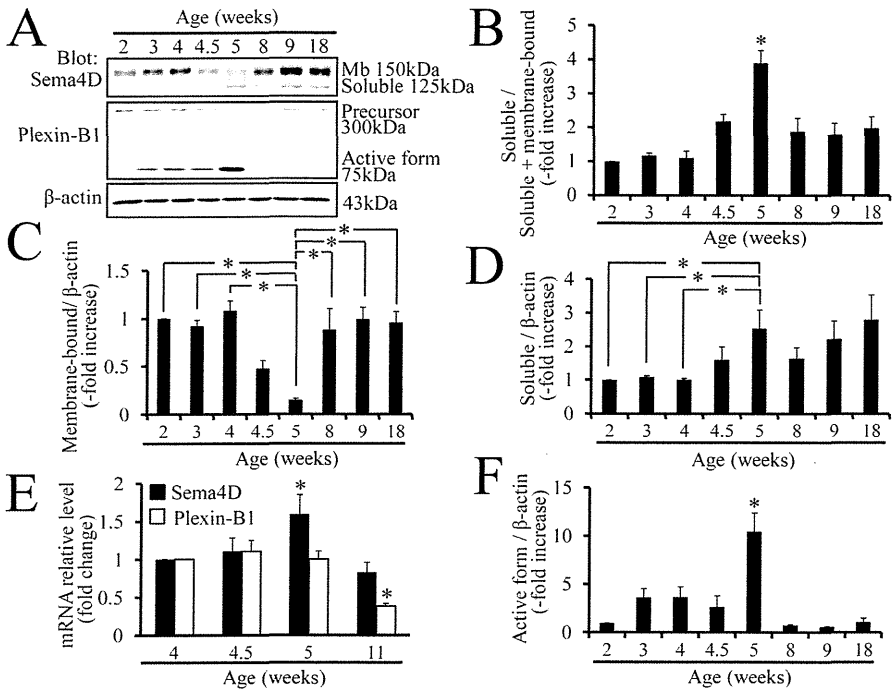

Figure 1. Increase of soluble Sema4D and reorganization of Plexin-B1 receptor during vaginal development. (A) The membrane-bound (larger) and soluble (smaller) forms of Sema4D are evident on western blots containing proteins from vaginal tissue extracts. The precursor (larger) and active form (smaller) of Plexin-B1 are also evident on western blots containing proteins from vaginal tissue extracts; the active 75 kDa form represents a fragment of the 300 kDa Plexin-B1 precursor produced by proprotein convertase. The fragments resulting from the proprotein convertase-dependent cleavage are integrated into signaling-active receptors, which have a distinct conformation from the precursors [20]. Age (weeks): vaginal protein extracts from 2-, 3-, 4-, 4.5-, 5-, 8-, 9-, or 18-week-old mice. Mb: membrane-bound. (B) The ratio of soluble Sema4D to total Sema4D increases significantly in 5-week-old mouse vaginal tissue. Each data point represents the mean ± SEM of 3 to 6 mice. *$P<0.05$, ANOVA. (C) The ratio of membrane-bound Sema4D to β-actin significantly decreases in 5-week-old vaginal tissue. Each column represents the mean ± SEM of 4 mice. *$P<0.05$, ANOVA. (D) The ratio of soluble Sema4D to β-actin in 5-week-old mouse vaginal tissue is significantly higher than that in 2-, 3-, or 4-week-old mouse vaginal tissue. Each value represents the mean ± SEM of 3 to 6 mice. *$P<0.05$, ANOVA. (E) Based on real-time PCR data, the expression of Sema4D mRNA increases significantly in vaginal tissue from 5-week-old mice as compared with that from any other developmental stage. Plexin-B1 mRNA levels show no changes during vaginal opening except for a significant decline in 11-week-old mice. Each column represents the mean ± SEM of 4 mice. *$P<0.05$, ANOVA. (F) The ratio of active Plexin-B1 to β-actin is significantly higher in 5-week-old mouse vaginal tissue than in that from any other developmental stage. Each point represents the mean ± SEM of 3 to 6 mice. *$P<0.05$, ANOVA.
doi:10.1371/journal.pone.0097909.g001

protein content in each tissue extract, and samples containing 15 μg of protein were prepared with a solution of 60 mM Tris-HCl (pH 6.8), 2% SDS, 10% glycerol, 0.1% bromophenol blue, and 5% β-mercaptoethanol; each of these samples was incubated at 100°C for 5 min and subjected to electrophoresis through a 10% SDS-polyacrylamide gel; separated proteins were then transferred to polyvinylidine difluoride membranes (Amersham Pharmacia Biotech, Buckinghamshire, UK). Sema4D, plexin-B1, cleaved caspase-3, Akt, phospho-Akt, ERK1/2, and phospho-ERK1/2 were detected with the respective antibodies and an ECL-plus or ECL Western blot detection system in accordance with the manufacturers' instructions (Amersham). The antibodies utilized were anti-CD100/Sema4D (BD Transduction Laboratories, NJ, USA), anti-plexin-B1 (Santa Cruz Biotechnology, Inc.), anti-cleaved caspase-3 (Cell Signaling Technology), anti-Akt (Cell Signaling Technology), anti-phospho-Akt (Cell Signaling Technology), anti-Erk1/2 (Cell Signaling Technology), anti-phospho-Erk1/2 antibody (Cell Signaling Technology), and β-actin antibody (Cell Signaling Technology).

Ovariectomy and Estrogen Supplementation

For each ovariectomy (OVX), both ovaries were excised from a 22-day-old mouse while the mouse was under anesthesia from intraperitoneal injection of pentobarbital sodium. As controls, sham operations, in which both ovaries were manipulated but not resected, were performed on WT or Sema4D−/− mice. Ovariectomized mice were then separated into three groups: in two groups, from postnatal day 24 to postnatal day 34, β-estradiol (E2, 0.1 μg/kg body weight, Sigma Chemical Co., St. Louis, MO) (OVX-E2 group) or vehicle oil (OVX-oil group) was injected daily and subcutaneously into each mouse, and in the remaining group, no injection was administered (OVX group). The OVX-E2 and OVX-oil groups were sacrificed for Western and immunohistochemical analysis 24 hours after the last injection. Both sham-operated and OVX mice were also sacrificed for Western and immunohistochemical analysis on postnatal day 35. Uterine weight of each mouse was measured to assess the effects of OVX, oil supplementation (OVX-oil) and estrogen supplementation (OVX-E2), as shown in Fig. S1.

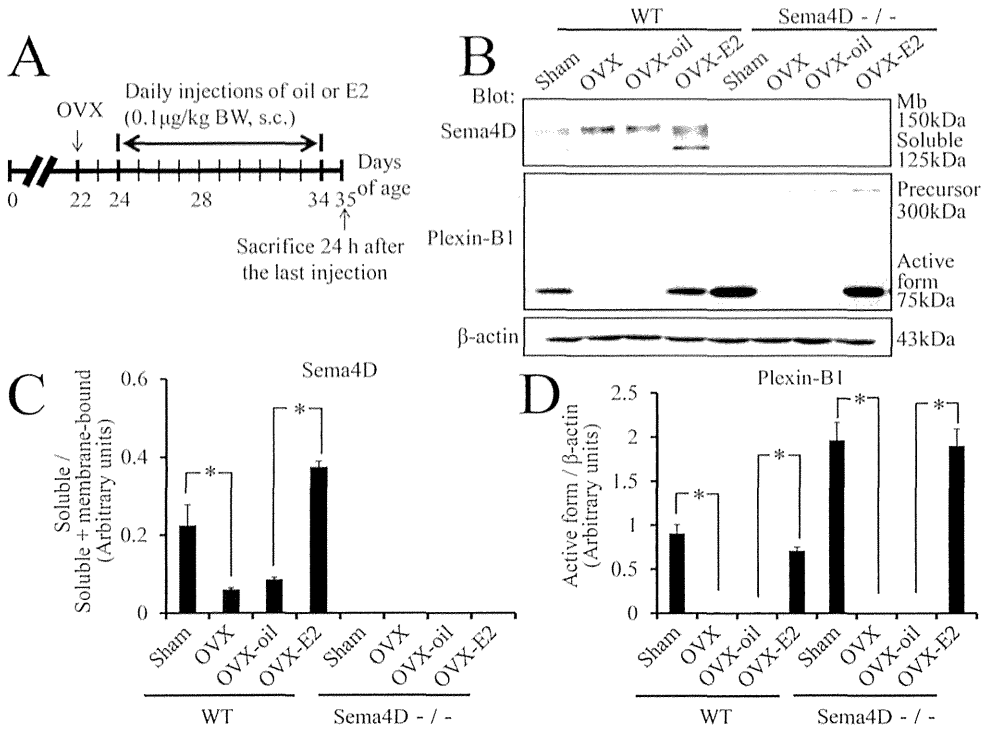

Figure 2. Hormonal regulation of structural changes in Sema4D and Plexin-B1. (A–D) To investigate whether estrogen induces structural changes in Sema4D, Plexin-B1, or both, ovariectomized mice receive daily subcutaneous injections (s.c.) of 17β-estradiol (E2, 0.1 μg/kg) until 5 weeks after birth. As expected, both soluble Sema4D and active Plexin-B1 are detected in vaginal tissue from sham-operated 5-week-old female WT mice (Sema4D+/+). Interestingly, after ovariectomy (OVX) and ovariectomy plus oil supplementation (OVX-oil), the amounts of both soluble Sema4D and active Plexin-B1 significantly decrease. The decrease in active protein levels is rescued by daily subcutaneous injection of E2 (OVX-E2); these findings indicate that the enzymes cleaving membrane-type Sema4D and Plexin-B1 precursor are induced by estrogen. In Sema4D−/− mice, OVX and OVX-oil result in significant decreases in the active form of Plexin-B1; these decreases are abrogated by OVX-E2 treatment. Both membrane-bound and soluble Sema4D are not evident in samples from Sema4D−/− mice. Each value in the graphs (C, D) represents the mean ± SEM of 5 mice. *$P<0.05$, ANOVA.
doi:10.1371/journal.pone.0097909.g002

Real-time RT-PCR

The SV Total RNA Isolation System (Promega, Madison, WI) was used according to the manufacturer's instructions to extract RNA from vaginal tissues of sham-operated WT and Sema4D−/− mice, as well as from OVX, OVX-oil, and OVX-E2 mice. Total RNA was extracted from developing vaginal tissues via the same procedure. The QuantiTect Primer Assays and the following probes Mm_Sema4d_1_SGQT00115206, Mm_Plxnb1_1_SG QT00126483, Mm_B2m_2_SG QT01149547 (Qiagen, Tokyo, Japan) were used according to the manufacturer's instructions to perform real-time RT-PCR.

Statistics

Each data value was expressed as a mean ± standard error of the mean (SEM). Comparisons between WT and Sema4D−/− mice were conducted with the Student's t-test or a one-way or two-way analysis of variance (ANOVA) followed by a *post hoc* test. A level of $p<0.05$ was considered statistically significant.

Results

Conversion of Membrane-bound Sema4D to Soluble Secreted Sema4D during Vaginal Development

Western blots were probed with anti-Sema4D antibodies to examine the expression patterns of membrane-bound and soluble secreted Sema4D during vaginal development; samples of tissue extracts were taken from each stage of postnatal mouse vaginal development. The ratio of soluble to total Sema4D was significantly higher 5 weeks after birth, which is when vaginal opening occurs, than at any other developmental stage (Fig. 1A, B). Membrane-bound Sema4D level was significantly lower at 5 weeks after birth than at any other developmental stage (Fig. 1C). The results illustrated that the rate of conversion from membrane-bound Sema4D to secreted Sem4D was significantly higher at the time of vaginal opening than at any other developmental stage.

Concordant with the significantly higher level of soluble secreted Sema4D in 5-week-old vaginal tissues, the *Sema4D* mRNA level was also significantly higher in 5-week-old vagina tissue based on real-time RT-PCR analysis (Fig. 1E).

Reorganization of Plexin-B1 during Vaginal Development

Western blots were probed with anti-Plexin-B1 antibodies to examine whether the expression of the Sema4D receptor, Plexin-B1, changed during vaginal development. Vaginal tissue protein extracts from each developmental stage and anti-Plexin-B1 antibodies that detected both a 300 kDa form and a smaller 75 kDa form were used for this analysis (Fig. 1A). The 300 kDa protein represents the precursor form of Plexin-B1 that exists prior to digestion by a protease, proprotein convertase [20]. The smaller 75 kDa protein represents the Plexin-B1 fragment that is

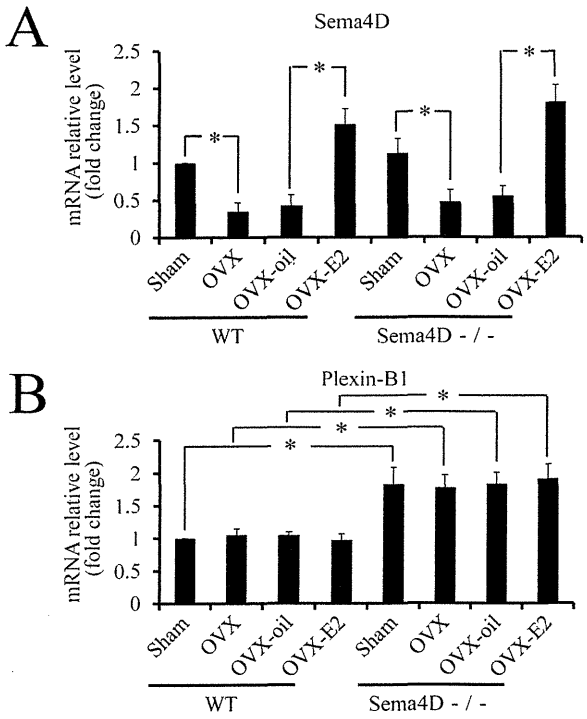

Figure 3. Estrogen increases levels of *Sema4D* mRNA, but not *Plexin-B1* mRNA in mouse vagina. (A) *Sema4D* mRNA levels were significantly lower in vaginal tissues from OVX WT mice than in vaginal tissues from sham-operated mice. Based on comparisons between OVX-E2 and OVX-oil mice, OVX-E2 treatment induced a significant increase of *Sema4D* mRNA levels in WT vaginal tissues. The *Sema4D* mRNA variant transcribed in Sema4D−/− mice, but not translated into Sema4D protein exhibits an expression pattern similar to that of wild-type *Sema4D* mRNA. Each value represents the mean ± SEM of 5 mice. *$P<$ 0.05, ANOVA. (B) *Plexin-B1* mRNA levels in vaginal tissues from any Sema4D−/− mice group were significantly higher than those in vaginal tissues from any WT mice group. In WT or Sema4D−/− mice, any treatment does not induce any significant alteration of *Plexin-B1* mRNA levels in vaginal tissues. Each value represents the mean ± SEM of 5 mice. *$P<0.05$, ANOVA.
doi:10.1371/journal.pone.0097909.g003

generated by proprotein convertase-mediated digestion [20]. After convertase-mediated digestion of the Plexin-B1 precursor, the conformation of Plexin-B1 protein structure is transformed into an active form that transmits Sema4D signal more intensely (20, Fig. S2). Interestingly, the ratio of the smaller 75 kDa band to the β-actin band was significantly higher for the 5-week sample than for any other sample (Fig. 1F). Thus the western blot findings indicated that the active form of Plexin-B1 was highest at 5 weeks, which is the time of mouse vaginal opening. Real-time PCR analysis demonstrated that *Plexin-B1* mRNA levels were constant during postnatal vaginal development except that the mRNA declined significantly by the 11th week (Fig. 1E).

Conversion of Sema4D and of Plexin-B1 is Estrogen-dependent

Postnatal vaginal remodeling in mice is a hormonally triggered process [1]; therefore, we investigated whether proteolytic release of Sema4D and reorganization of Plexin-B1 during remodeling were each estrogen dependent. Mice were initially subjected to ovariectomy on postnatal day 22; one third of these mice were each injected with exogenous estrogen (OVX-E2 mice), another third with vehicle only (OVX-oil mice, Fig. 2A) and the remaining third received no injection (OVX mice). Western blot analysis was used to examine both Sema4D proteolysis and Plexin-B1 conversion in these ovariectomized mice when the mice became 5 weeks old (Fig. 2B). Conversion of membrane-bound Sema4D into the soluble form was significantly lower in OVX mice than in sham-operated WT mice (Fig. 2B, C). In contrast, this Sema4D conversion was significantly higher in WT OVX-E2 than in WT OVX-oil mice (Fig. 2B, C); these findings indicated that proteolytic conversion of Sema4D was estrogen dependent. Reorganization of Plexin-B1 into an active form was significantly lower in WT OVX mice than in sham-operated WT mice (Fig. 2B, D). The reorganization of Plexin-B1 was significantly higher in WT OVX-E2 mice than in WT OVX-oil mice; these findings indicated Plexin-B1 reorganization during mouse vaginal tissue remodeling was estrogen dependent (Fig. 2B, D). The phenomenon was also confirmed in Sema4D−/− mice (Fig. 2B, D).

To examine whether OVX and OVX-E2 treatment affected *Sema4D* or *Plexin-B1* mRNA expression, or both, *Sema4D* and *Plexin-B1* mRNA levels in vaginal tissues were quantified via real-time RT-PCR for sham-operated WT and Sema4D−/− mice, as well as OVX mice, OVX-oil mice and OVX-E2 mice. *Sema4D* mRNA levels in vaginal tissues from WT OVX mice were significantly lower than in vaginal tissues from WT sham-operated mice. Conversely, *Sema4D* mRNA levels were significantly higher in vaginal tissues from OVX-E2 WT mice than vaginal tissues from OVX or OVX-oil mice (Fig. 3A); these findings indicated that estrogen mediated transcriptional modulation of *Sema4D* gene. Real-time PCR with forward and reverse primers corresponding to nucleotide sequences in the second and third exons of the *Sema4D* gene, respectively, detected a *Sema4D* mRNA variant in Sema4D−/− vagina tissues (Fig. 3A). The *Sema4D* mRNA variant did not contain the region transcribed from the coding sequences in the first exon of the *Sema4D* gene because the coding sequences covering the translation-initiation codon are not found in the Sema4D−/− mice genome [21]. Thus, the *Sema4D* mRNA variant was not translated to Sema4D protein. Indeed, the Sema4D protein could not be detected in the Sema4D−/− vagina (Fig. 2B, C) or in Sema4D−/− immune cells [21]. Levels of this mRNA variant were significantly higher in Sema4D−/− vaginal tissues from OVX-E2 mice than in vaginal tissues from OVX or OVX-oil mice (Fig. 3A); these findings indicated that estrogen mediated transcriptional modulation of this *Sema4D* mRNA variant. *Plexin-B1* mRNA levels in vaginal tissues from sham-operated Sema4D−/− mice, as well as OVX, OVX-oil, and OVX-E2 mice, were significantly higher than *Plexin-B1* mRNA levels in any WT group (Fig. 3B). However, neither OVX nor OVX-E2 treatment significantly altered *Plexin-B1* mRNA levels in the vaginal tissues of WT or Sema4D−/− mice (Fig. 3B). Thus, the increase of Plexin-B1 reorganization into an active form in vaginal tissues of OVX-E2 mice resulted from an increase in the estrogen-dependent cleavage of Plexin-B1 precursor.

Sema4D is Integral for Estrogen-dependent Vaginal Epithelial Apoptosis *In vivo*

To determine whether Sema4D is essential to vaginal epithelial apoptosis *in vivo*, we measured and compared apoptosis in WT and Sema4D−/− mice; these mice were ovariectomized or sham-operated 3 weeks after birth and then treated with estrogen or vehicle until 5 weeks after birth. Caspase-3 activation was used to measure vaginal apoptosis, and caspase-3 activation was significantly higher in WT OVX-E2 mice than in WT OVX-oil mice (Fig. 4A, C). In contrast, based on both western blot analysis and

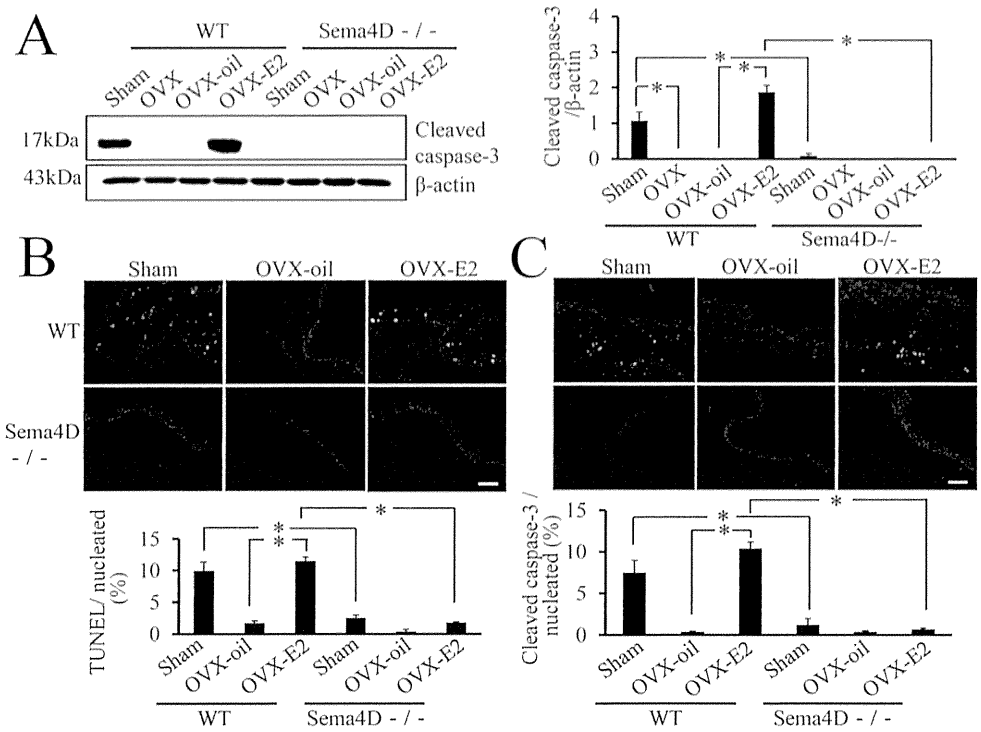

Figure 4. Essential role of Sema4D in estrogen-mediated vaginal apoptosis. (A) Both OVX and OVX-oil treatment of WT (Sema4D+/+) mice result in a significant decrease in cleaved caspase-3 level in vaginal tissue relative to cleaved caspase-3 levels in sham-operated mice (Sham). All vaginal tissue samples were taken from 5-week-old mice. Levels of cleaved caspase-3 were significantly higher in vaginal tissues from WT OVX-E2 mice than in vaginal tissues from WT OVX or WT OVX-oil mice. Levels of cleaved caspase-3 in vaginal tissue did not differ among OVX, OVX-E2, and OVX-oil Sema4D−/− mice; these findings indicate that Sema4D is essential to estrogen-mediated vaginal apoptosis. Each value represents the mean ± SEM of 5 mice. *$P<0.05$, ANOVA. (B, C) Both TUNEL assays and cleaved caspase-3 immunohistochemistry with vaginal tissue sampled from sham-operated (Sham) 5-week-old WT female (Sema4D+/+) mice show that the number of apoptotic epithelial cells is significantly larger than that in samples from Sham-treated Sema4D−/− mice. OVX-oil treatment of WT mice significantly decreases apoptotic cell number in 5-week-old vaginal epithelia relative to that in Sham; compared with OVX-oil treatment, OVX-E2 treatment of WT mice induces a significant increase in apoptotic cell number in 5-week-old vaginal epithelia, comparable to the level of Sham. OVX-E2 treatment does not induce significant apoptosis in 5-week-old vaginal epithelia of Sema4D−/− mice. Data are shown as means ± SEM; n = 5 per group.
doi:10.1371/journal.pone.0097909.g004

immunohistochemistry, vaginal apoptosis in ovariectomized Sema4D−/− mice remained low even in Sema4D−/− OVX-E2 mice (Fig. 4A, B, C). The results indicated that Sema4D was essential for estrogen-dependent vaginal epithelial cell apoptosis *in vivo* during the postnatal vaginal tissue remodeling that occurs 5 weeks after birth.

Dephosphorylation of Akt and ERK at the Time of Vaginal Opening is an Estrogen-dependent, Sema4D-mediated Event in Vaginal Epithelium

The mechanism suppressing activation of Akt and ERK may operate downstream of semaphorin signaling [16,23]; therefore, we examined the localization of Akt and ERK in the mouse vagina. Immunohistochemical findings indicated that these molecules were present in vaginal epithelium of WT and of Sema4D−/− mice (Fig. 5A). To examine whether dephosphorylation of Akt and of ERK operates in vaginas of 5-week-old WT mice, we used western blots to measure phosphorylated and unphosphorylated forms of these proteins during mouse vaginal development. The levels of both p-Akt and p-ERK decreased significantly in vaginas of 5-week-old WT mice at the time of vaginal opening; these findings indicated that Sema4D signal suppressed phosphorylation-dependent activation of Akt and of ERK (Fig. 5B).

To examine whether the decreases in p-Akt and in p-ERK depended on Sema4D, we compared WT and Sema4D−/− mice with regard to the levels of p-Akt and p-ERK in vaginal epithelium 5 weeks after birth. Western blot analysis showed that p-Akt and p-ERK expression was significantly higher in the Sema4D−/− vaginal tissue than in WT vaginal tissue (Fig. 5C). Thus, Sema4D signal may induce dephosphorylation of Akt and ERK at the time of vaginal opening.

To determine whether the decreases in p-Akt and p-ERK expression in mouse vaginal tissue 5 weeks after birth are estrogen dependent and Sema4D mediated, we measured p-Akt and p-ERK levels in vaginal tissues from WT and from Sema4D−/− mice that had been ovariectomized or sham-operated 3 weeks after birth and treated with vehicle only or estrogen thereafter. In vaginal tissue of WT mice, p-Akt and p-ERK expression 5 weeks after birth was significantly higher in OVX mice than in sham-operated mice (Fig. 6). On western blots, p-Akt and p-ERK levels were significantly lower in vaginal tissues from 5-week-old WT OVX-E2 mice than in those from OVX mice or from OVX-oil mice (Fig. 6); these findings indicated that regulation of dephosphorylation of Akt and ERK was estrogen dependent. To

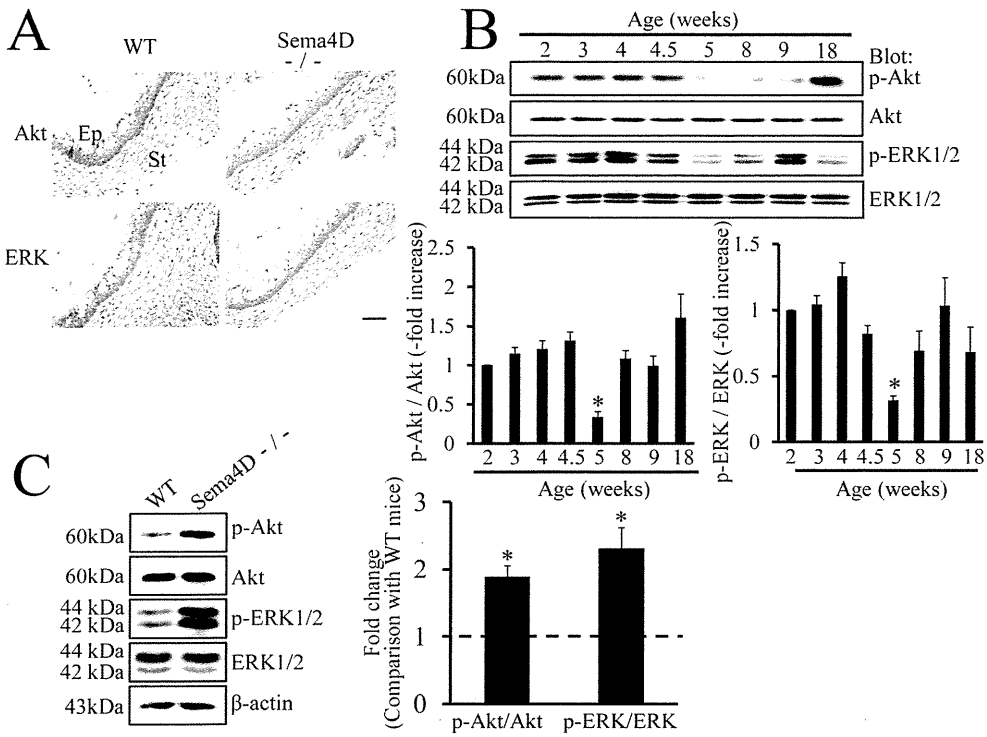

Figure 5. Dephosphorylation of Akt and ERK during vaginal opening. (A) Immunohistochemistry demonstrates that Akt and ERK are expressed in vaginal epithelium of both WT (Sema4D+/+) and Sema4D−/− mice at 5 weeks old at the time of vaginal opening. (B) Western blots show the expression patterns of Akt, ERK, and the respective phosphorylated forms during postnatal vaginal development in WT mice. Both pAkt and pERK levels are lower in samples from 5-week-old mice than in samples from any other stages of development. Age (weeks): vaginal protein extracts from 2-, 3-, 4-, 4.5-, 5-, 8-, 9-, or 18-week-old mice. Each value represents the mean ± SEM of 6 mice. *$P<0.05$, ANOVA. (C) Western blot analysis reveals significantly higher expression of pAkt and pERK in vaginal tissue samples from 5-week-old Sema4D−/− mice than in vaginal tissue samples from 5-week-old WT (Sema4D+/+) mice. The ratios of pAkt to Akt and separately of pERK to ERK were higher in vaginal tissue samples from 5-week-old Sema4D−/− than in vaginal tissue samples from WT mice. Data are shown as the mean ± SEM; n = 6 per mouse group. *$P<0.05$, Student's t-test.
doi:10.1371/journal.pone.0097909.g005

determine the extent to which this change in Akt and ERK phosphorylation depended on Sema4D, we examined tissues from Sema4D−/− mice. Notably, for Sema4D−/− mice, phosphorylation levels of Akt and ERK did not differ significantly among vaginal tissues from sham-operated, OVX, and OVX-oil mice (Fig. 6). However, Akt and ERK phosphorylation in vaginal tissue was significantly lower in Sema4D−/− OVX-E2 mice than in Sema4D−/− OVX-oil mice, but the Akt and ERK phosphorylation in Sema4D−/− OVX-E2 mice was significantly higher than that in WT OVX-E2 mice (Fig. 6). These results indicated that normal estrogen-dependent dephosphorylation of Akt and ERK at the time of vaginal opening was partially, but not completely, dependent on Sema4D.

Discussion

Using Sema4D−/− BALB/c mice, we documented three novel, crucial observations regarding the estrogen-dependent apoptosis that occurs during postnatal vaginal opening in mice. We found that 1) Sema4D, which is classified as a class 4 semaphorin, played an indispensable role as a downstream effector of estrogen action during apoptosis of vaginal epithelial cells as the vagina opens; 2) estrogen-dependent Sema4D processing and estrogen-dependent Plexin-B1 reorganization increased Sema4D signal transduction efficiency during vaginal opening; and 3) Sema4D contributed to estrogen-dependent attenuation of both Akt and ERK signaling during vaginal opening.

The high incidence of imperforate vagina and the prominent decrease in vaginal epithelial apoptosis during puberty in Sema4D−/− mice led to the hypothesis that Sema4D could induce apoptosis of vaginal epithelial cells. Our previous findings regarding Sema4D−/− vaginal epithelial cells in culture demonstrate the apoptosis-inducing activity of Sema4D [7]. Similarly, Sema3A, a member of class 3 semaphorins, induces apoptosis of kidney podocytes [24]. Notably, Sema4D could promote apoptosis of oligodendrocytes to control the differentiation of oligodendrocytes [25]. Furthermore, Sema3A has been implicated in Fas-mediated apoptosis; specifically, it may help the Fas molecule migrate into lipid rafts [26]. Thus, semaphorins exhibit crucial roles not only in axon guidance, but also in induction of apoptosis during development. However, the receptor and signal transduction machinery involved in semaphorin-mediated apoptosis have not been explored in detail. Our previous findings indicate that Plexin-B1 is involved in Sema4D-induced apoptosis of vaginal epithelial cells in culture [7]. In WT ovariectomized mice, apoptosis in vaginal epithelia was significantly higher in the OVX-E2 mice than in vehicle-treated ovariectomized mice (Fig. 4). In contrast, OVX-E2 treatment did not induce significant apoptosis in 5-week-old vaginal epithelia of Sema4D−/− mice (Fig. 4). Thus, these data indicated that Sema4D functioned as an essential downstream effector of estrogen action mediating vaginal

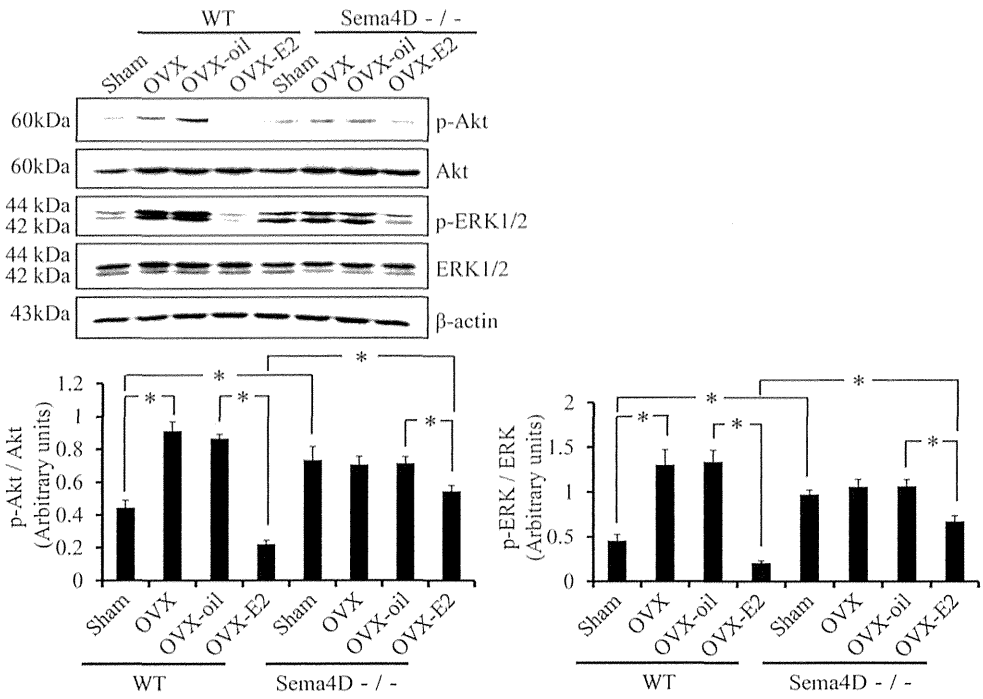

Figure 6. Sema4D contributes to the estrogen-dependent dephosphorylation of Akt and ERK during mouse vaginal opening. Western blot shows that ovariectomy (OVX) and ovariectomy plus oil (OVX-oil) both increase the phosphorylation level of Akt and ERK1/2 in vaginal tissue from 5-week-old WT (Sema4D+/+) mice. β-estradiol (E2) supplementation after ovariectomy (OVX-E2) induces significant dephosphorylation of Akt and ERK1/2 in vaginal tissue from 5-week-old WT mice. OVX and OVX-oil do not significantly increase phosphorylation of Akt and ERK1/2 in vaginal tissue from 5-week-old Sema4D−/− mice relative to that in sham-operated mice (Sham). OVX-E2 induces weak but significant dephosphorylation of Akt and ERK in vaginal tissue from 5-week-old Sema4D−/− mice. Dephosphorylation levels in the Sema4D−/− vagina is significantly lower than that in the WT vagina. Each data point represents the mean ± SEM of 3 to 6 mice. *$P<0.05$, ANOVA.
doi:10.1371/journal.pone.0097909.g006

epithelial apoptosis *in vivo* during postnatal tissue remodeling. Thus, this is the first manuscript reporting that a semaphorin known as an axon guidance molecule exhibited a decisive role in the downstream effects of estrogen action in the process of mouse vaginal opening [1]. Our study of ovariectomized mice further revealed that Sema4D was involved in the estrogen-dependent dephosphorylation of pAkt and pERK in postnatal vaginal tissue remodeling (Fig. 6). Similar to the signal transduction pathway of Sema4D that functions in neuronal growth cone guidance [14,15,16], the Sema4D pathway in vaginal epithelium may involve dephosphorylation of pAkt and pERK; this dephosphorylation may depend on downregulation of Ras family members; this Ras family downregulation may in turn be caused by Plexin-B1 GAP activities that are activated by Sema4D signal in vaginal epithelial apoptosis during vaginal opening in mice.

Conversion of membrane-bound Sema4D to secreted Sema4D was significantly higher during vaginal opening than during any other period of development (Fig. 1A, B, C, D). The increase in the conversion of membrane-bound Sema4D to secreted Sema4D may facilitate induction of apoptosis by increasing the activity of Sema4D as a ligand that acts on both neighboring and distant cells [19]. Sema4D mRNA levels peaked in vaginal epithelium 5 weeks after birth (Fig. 1E); this increase may have boosted apoptosis by increasing ligand quantity. Based on comparisons between OVX-E2 and OVX-oil mice, OVX-E2 treatment induced a significant increase in *Sema4D* mRNA levels in mouse vagina (Fig. 3A), indicating that estrogen may have modulated transcription of the *Sema4D* gene. Since the ratio of soluble Sema4D to total Sema4D increased in concert with the increase of *Sema4D* mRNA in vaginal tissues of WT OVX-E2 mice (Fig. 2B, C), the significant increase in soluble Sema4D in OVX-E2 mice relative to that in OVX-oil mice resulted from enhanced estrogen-dependent cleavage of membrane-bound Sema4D to soluble Sema4D in vaginal tissues in OVX-E2 mice relative to that in OVX-oil mice. Accordingly, experiments involving ovariectomy demonstrated that the conversion from membrane-bound to secreted Sema4D was estrogen dependent (Fig. 2B, C); therefore, the activities and/or amounts of cleavage enzyme releasing soluble Sema4D by cutting membrane-bound Sema4D may increase in response to the estrogen increase at the time of vaginal opening. Although a previous study reported that the function of the cleavage enzyme is to produce the secreted form of Sema4D by cutting membrane-bound Sema4D during T cell activation in the immune system [19], the present study is the first to demonstrate the estrogen-dependent conversion of Sema4D from a membrane-bound precursor to a secreted protein.

Expression of a short fragment of Plexin-B1 that results from enzyme-dependent proteolysis of a Plexin-B1 precursor peaked at the time of vaginal opening; this pattern was similar to the pattern of soluble Sema4D production (Fig. 1A, F). Research with human cell lines showed that a proprotein convertase cleaves the precursor of Plexin-B1 and results in a conformational change of the Plexin-B1 molecule and enhancement of Plexin-B1-mediated signal transduction [20]. Sites that contain the amino acid sequence RXXR and that may be recognized by proprotein convertases actually reside in the mouse Plexin-B1 molecule (R_{546}EERR and R_{1169}GPR, Figure S2). The predicted molecular

size of the cleavage Plexin-B1 molecule produced by proprotein convertases coincides with the size actually detected on western blots probe with anti-Plexin-B1 antibodies (Fig. 1A, Figure S2). The activated form of Plexin-B1, structurally modified and activated for signaling by the proteolytic cleavage, increased most in amount at the time of vaginal opening; this proteolytic conversion may have accelerated vaginal epithelial apoptosis by enhancing signal transduction of Sema4D. Conversion of Plexin-B1 precursor into active Plexin-B1 in mouse vaginal tissue was estrogen dependent (Fig. 1A, Fig. 2B, D); therefore, the amounts and/or activities of the proprotein convertases that cleave Plexin-B1 may also increase in an estrogen-dependent manner. Even though the receptor activation that is mediated by the proteolytic cleavage of Plexin-B1 was previously observed in several cultured cell lines [20], our study is the first to demonstrate the estrogen dependency of the proteolytic conversion of Plexin-B1 during mouse vaginal opening.

C57BL/6 Sema4D−/− mice do not exhibit a high incidence of imperforate vagina, but BALB/c Sema4D−/− mice do. LH-RH neuron precursor cells in C57BL/6 Sema4D−/− mice exhibit defective migration from the olfactory placode to the hypothalamus during embryonic brain development [27]. A significant decrease in secondary ovarian follicles is also evident in Sema4D−/− C57BL/6 mice [28]. Our previous study revealed no significant difference in serum estrogen levels between Sema4D−/− BALB/c mice and WT mice 5 weeks after birth. [7]. Since injection of β-estradiol into infant Sema4D−/− mice does not lead to vaginal opening, the possibility that vaginal atresia in pubescent Sema4D−/− mice was caused by insufficient secretion of estrogen was excluded [7]. Further experiments involving ovariectomy, estrogen supplementation, and WT and Sema4D−/− BALB/c mice clearly revealed that the Sema4D was essential to vaginal epithelial apoptosis, which was regulated by the estrogen present during vaginal opening (Fig. 4A, B, C). Previous findings indicate that Plexin-B1 is the receptor that induces apoptosis of vaginal epithelial cells in culture [7]; however, a closed vaginal phenotype has not been reported in Plexin-B1−/− C57BL/6 mice [29,30]. Future experiments may be necessary to examine whether the closed vaginal phenotype also occurs in BALB/c mice lacking Plexin-B1. The structural conversion of Sema4D and of Plexin-B1 that was evident in BALB/c mice was also evident in C57BL/6 mice during postnatal vaginal development (Fig. S3). However, the day of vaginal opening (5 weeks old) coincided with the peak in the conversion of both Sema4D and Plexin-B1 in BALB/c mice, (Figure 1), but there was no concordance between the day of vaginal opening (37.18 ± 0.787 day old, $n = 17$) and the peak of the proteolytic conversions (24 to 28 days old) in C57BL/6 mice (Fig. S3). These observations may illustrate that postnatal vaginal tissue remodeling processes are more dependent on Sema4D/Plexin-B1 signal transduction system in BALB/c mice than in C57BL/6 mice.

Thus, we propose that extensive apoptosis that occurs in epithelial cells in the vaginal cavity during postnatal vaginal opening in BALB/c mice is induced by Sema4D–Plexin-B1 signaling and that this signaling is enhanced by the estrogen-dependent increase in both soluble Sema4D and active Plexin-B1 5 weeks after birth.

Supporting Information

Figure S1 Confirmation of the effect of ovariectomy and estrogen supplementation. Both ovariectomized (OVX) WT (Sema4D+/+) and Sema4D−/− mice exhibit a significant decrease in uterine weight when compared with sham-operated animals. WT and Sema4D−/− mice with ovariectomy and estrogen supplementation (OVX-E2) exhibit significant increases in uterine weight when compared with ovariectomized mice supplemented with oil (OVX-oil). Values shown are mean ± SEM. *$P<0.05$. OVX, ovariectomy; OVX-oil, ovariectomy plus oil supplementation; OVX-E2, ovariectomy plus 17β-estradiol supplementation.
(TIF)

Figure S2 The sites of Plexin-B1 cleaved by proprotein convertase. Plexin-B1, the Sema4D receptor, transforms from a precursor protein into an active protein via a conformational change that is caused by proprotein convertase-dependent cleavage of Plexin-B1. The proprotein convertase recognizes and cleaves the RXXR sequence residing in the target protein. A protein fragment presumed to result from the cleavage of R_{546}EERR and R_{1169}GPR of mouse Plexin-B1 is detected as a 75 kDa band on the western blot probed with anti-Plexin-B1 antibody (A-8). A-8 is a monoclonal antibody raised against the peptide fragment comprising amino acids 771-1070 of human plexin-B1, which is highly conserved with mouse plexin-B1 and covered by the 75 kDa region detected by western blot with A8. A previous study showed that the region covering the transmembrane and intracellular region, which is generated by proprotein convertase-mediated digestion of mouse plexin-B1, has a molecular size of 150 kDa [30]. EC: extracellular domain, TM: transmembrane domain, IC: intracellular domain, PCs: proprotein convertases.
(TIF)

Figure S3 Conversion of Sema4D and Plexin-B1 into respective soluble and active form during C57BL/6 vaginal development. The conversion of both Sema4D and Plexin-B1 into the respective soluble and active forms peaked 3.5 to 4 weeks (24 to 28 days) after birth; this time period does not coincide with the vaginal opening in C57BL/6 mice (37 days old).
(TIF)

Acknowledgments

We would like to thank all members of the Department of Physiology at Meijo University for their enthusiastic discussion and invaluable assistance.

Author Contributions

Conceived and designed the experiments: TI TT TK HK AK K. Yukawa. Performed the experiments: TI TB TT K. Yoshida TU TN. Analyzed the data: TI TB TT K. Yoshida TN K. Yukawa. Contributed reagents/materials/analysis tools: MM HT. Wrote the paper: TI K. Yukawa.

References

1. Rodriguez I, Araki K, Khatib K, Martinou JC, Vassalli P (1997) Mouse vaginal opening is an apoptosis-dependent process which can be prevented by overexpression of Bcl2. Dev. Biol. 184: 115–121.
2. Hübner A, Cavanagh-Kyros J, Rincon M, Flavell RA, Davis RJ (2010) Functional cooperation of the proapoptotic Bcl2 family proteins Bmf and Bim in vivo. Mol. Cell. Biol. 30: 98–105.
3. Lindsten T, Ross AJ, King A, Zong W-X, Rathmell JC, et al. (2000) The combined functions of proapoptotic Bcl-2 family members Bak and Bax are essential for normal development of multiple tissues. Mol. Cell 6: 1389–1399.
4. Simpson KJ, Wati MR, Deans AJ, Lindeman GJ, Brown MA (2004) MMTV-trBrca1 mice display strain-dependent abnormalities in vaginal development. Int. J. Dev. Biol. 48: 675–678.
5. Cano-Gauci DF, Song HH, Yang H, McKerlie C, Choo B, et al. (1999) Glypican-3-deficient mice exhibit developmental overgrowth and some of the

abnormalities typical of Simpson-Golabi-Behmel syndrome. J. Cell Biol. 146: 255–264.
6. Sundberg JP, Brown KS (1994) Imperforate vagina and mucometra in inbred laboratory mice. Laboratory Animal Science 44: 380–382.
7. Ito T, Bai T, Tanaka T, Yoshida K, Ueyama T, et al. (2014) Semaphorin 4D induces vaginal epithelial apoptosis to control mouse postnatal vaginal tissue remodeling. Mol Med Rep. in press.
8. Pasterkamp RJ (2012) Getting neural circuits into shape with semaphorins. Nat. Rev. Neurosci. 13: 605–618.
9. Kruger RP, Aurandt J, Guan KL (2005) Semaphorins command cells to move. Nat. Rev. Mol. Cell Biol. 6: 789–800.
10. Semaphorin Nomenclature Committee (1999) Unified nomenclature for the semaphorins/collapsins. Cell 97: 551–552.
11. Swiercz JM, Kuner R, Behrens J, Offermanns S (2002) Plexin-B1 directly interacts with PDZ-RhoGEF/LARG to regulate RhoA and growth cone morphology. Neuron 35: 51–63.
12. Nakamura F, Kalb RG, Strittmatter SM (2000) Molecular basis of semaphorin-mediated axon guidance. J. Neurobiol. 44: 219–229.
13. Janssen BJ, Robinson RA, Pérez-Branguli F, Bell CH, Mitchell KJ, et al. (2010) Structural basis of semaphorin-plexin signaling. Nature 467: 1118–1122.
14. Oinuma I, Ishikawa Y, Katoh H, Negishi M (2004) The semaphorin 4D receptor plexin-B1 is a GTPase activating protein for R-Ras. Science 305: 862–865.
15. Saito Y, Oinuma I, Fujimoto S, Negishi M (2009) Plexin-B1 is a GTPase activating protein for M-Ras, remodeling dendrite morphology. EMBO Rep. 10: 614–621.
16. Ito Y, Oinuma I, Katoh H, Kaibuchi K, Negishi M (2006) Sema4D/Plexin-B1 activates GSK-3β through R-Ras GAP activity, inducing growth cone collapse. EMBO Rep. 7: 704–709.
17. Basile JR, Afkhami T, Gutkind JS (2005) Semaphorin 4D/Plexin-B1 induces cell migration through the activation of PYK2, Src, and the phosphatidylinositol 3-kinase-Akt pathway. Mol. Cell. Biol. 25: 6889–6898.
18. Basile JR, Gavard J, Gutkind JS (2007) Plexin-B1 utilizes RhoA and Rho kinase to promote the integrin-dependent activation of Akt and ERK and endothelial cell motility. J. Biol. Chem. 282: 34888–34895.
19. Elhabazi A, Delaire S, Bensussan A, Boumsell L, Bismuth G (2001) Biological activity of soluble CD100. I. The extracellular region of CD100 is released from the surface of T lymphocytes by regulated proteolysis. J. Immunol. 166: 4341–4347.
20. Artigiani S, Barberis D, Fazzari P, Longati P, Angelini P, et al. (2003) Functional regulation of semaphorin receptors by proprotein convertases. J. Biol. Chem. 278: 10094–10101.
21. Shi W, Kumanogoh A, Watanabe C, Uchida J, Wang X, et al. (2000) The class IV semaphoring CD100 plays nonredundant roles in the immune system: defective B and T cell activation in CD100-deficient mice. Immunity 13: 633–642.
22. Li L, Tanaka T, Yukawa K, Akira S, Umesaki N (2009) Irinotecan-induced ovarian follicular apoptosis is attenuated by deleting the kinase domain of death-associated protein kinase. Int. J. Oncol. 34: 905–914.
23. Atwal JK, Singh KK, Tessier-Lavigne M, Miller FD, Kaplan DR (2003) Semaphorin 3F antagonizes neurotrophin-induced phosphatidylinositol 3-kinase and mitogen-activated protein kinase signaling: A mechanism for growth cone collapse. J. Neurosci. 23: 7602–7609.
24. Guan F, Villegas G, Teichman J, Mundel P, Tufro A (2006) Autocrine class 3 semaphorin system regulates slit diaphragm proteins and podocyte survival. Kidney Int. 69: 1564–1569.
25. Yamaguchi W, Tamai R, Kageura M, Furuyama T, Inagaki S (2012) Sema4D as an inhibitory regulator in oligodendrocyte development. Mol. Cell. Neurosci. 49: 290–299.
26. Moretti S, Procopio A, Lazzarini R, Rippo MR, Testa R, et al. (2008) Semaphorin3A signaling controls Fas (CD95)-mediated apoptosis by promoting Fas translocation into lipid rafts. Blood 111: 2290–2299.
27. Giacobini P, Messina A, Morello F, Ferraris N, Corso S, et al. (2008) Semaphorin 4D regulates gonadotropin hormone-releasing hormone-1 neuronal migration through PlexinB1-Met complex. J. Cell Biol. 183: 555–566.
28. Dacquin R, Domenget C, Kumanogoh A, Kikutani H, Jurdic P, et al. (2011) Control of bone marrow resorption by semaphorin 4D is dependent on ovarian function. PLoS ONE 6: e26627.
29. Hirschberg A, Deng S, Korostylev A, Paldy E, Costa MR, et al. (2010) Gene deletion mutants reveal a role for semaphorin receptors of the plexin-B family in mechanisms underlying corticogenesis. Mol. Cell. Biol. 30: 764–780.
30. Fazzari P, Penachioni J, Gianola S, Rossi F, Eickholt BJ, et al. (2007) Plexin-B1 plays a redundant role during mouse development and in tumour angiogenesis. BMC Dev. Biol. 7: 55.

OPEN ACCESS Freely available online

PLOS ONE

^{11}C-Acetate PET Imaging in Patients with Multiple Sclerosis

Kazushiro Takata[1☯], Hiroki Kato[2☯], Eku Shimosegawa[2], Tatsusada Okuno[1], Toru Koda[1], Tomoyuki Sugimoto[3], Hideki Mochizuki[1], Jun Hatazawa[2,4*], Yuji Nakatsuji[1*]

1 Department of Neurology, Osaka University Graduate School of Medicine, Suita, Osaka, Japan, **2** Department of Nuclear Medicine and Tracer Kinetics, Osaka University Graduate School of Medicine, Suita, Osaka, Japan, **3** Hirosaki University Graduate School of Science and Technology, Hirosaki, Aomori, Japan, **4** WPI-Immunology Frontier Research Center, Osaka University, Suita, Osaka, Japan

Abstract

Background: Activation of glial cells is a cardinal feature in multiple sclerosis (MS) pathology, and acetate has been reported to be selectively uptaken by astrocytes in the CNS. The aim of this study was to investigate the efficacy of PET with ^{11}C-acetate for MS diagnosis.

Materials and Methods: Six patients with relapsing-remitting MS and 6 healthy volunteers (HV) were enrolled. The ^{11}C-acetate brain uptake on PET was measured in patients with MS and HV. Volume-of-interest analysis of cerebral gray and white matter based on the segmentation technique for co-registered MRI and voxel-based statistical parametric analysis were performed. Correlation between ^{11}C-acetate uptake and the lesion number in T1- and T2- weighted MR images were also assessed.

Results: The standardized uptake value (SUV) of ^{11}C-acetate was increased in both white and gray matter in MS patients compared to HV. Voxel-based statistical analysis revealed a significantly increased SUV relative to that in the bilateral thalami (SUVt) in a broad area of white matter, particularly in the subcortical white matter of MS patients. The numbers of T2 lesions and T1 black holes were significantly correlated with SUV of ^{11}C-acetate in white and gray matter.

Conclusions: The ^{11}C-acetate uptake significantly increased in MS patients and correlated to the number of MRI lesions. These preliminary data suggest that ^{11}C-acetate PET can be a useful clinical examination for MS patients.

Citation: Takata K, Kato H, Shimosegawa E, Okuno T, Koda T, et al. (2014) ^{11}C-Acetate PET Imaging in Patients with Multiple Sclerosis. PLoS ONE 9(11): e111598. doi:10.1371/journal.pone.0111598

Editor: Akio Suzumura, Research Inst. of Environmental Med., Nagoya Univ., Japan

Received August 21, 2014; **Accepted** September 25, 2014; **Published** November 4, 2014

Data Availability: The authors confirm that all data underlying the findings are fully available without restriction. All relevant data are within the paper and its Supporting Information files.

Funding: This study was supported by the Health and Labor Sciences Research Grants from the Ministry of Health, Labor and Welfare of Japan, by a Grant-in-Aid for Scientific Research of Japan Society for the Promotion of Science (YN and TO) and by the Japan Society for the Promotion of Science KAKENHI Grant Number 23592089 (HK). The funders had no role in study design, data collection and analysis, decision to publish, or preparation of the manuscript.

Competing Interests: The authors have declared that no competing interests exist.

* Email: hatazawa@tracer.med.osaka-u.ac.jp (JH); yuji@neurol.med.osaka-u.ac.jp (YN)

☯ These authors contributed equally to this work.

Introduction

Multiple sclerosis (MS) is an inflammatory demyelinating autoimmune disease of the CNS [1]. Although MRI is recognized as the most informative surrogate marker [2], the diagnostic value of MRI in MS remains insufficient [3]. Glial activation is a key feature in the neuroinflammatory MS pathology, and glial activation from the early phase of MS is suggested by a MRS study [4]. Microglial activation has also been shown in PET studies [5,6]. However, astrocyte activation in MS has not been evaluated in vivo due to the lack of an appropriate radioligand, despite the astrocytosis observed from the early phase of disease and the important role potentially played by astrocytes [4,7,8].

Acetate is converted into fatty acids by the key enzyme acetyl-CoA synthase and metabolized in the citric acid cycle. ^{11}C-acetate has been used as a tracer to evaluate cardiac oxidative metabolism [9] and later used as a PET biomarker in patients with renal cell carcinoma, hepatocellular carcinoma, prostate cancer, and multiple myeloma [10,11,12,13]. In the CNS, ^{11}C-acetate PET has proven useful for the diagnosis of astrocytoma [14] because acetate is preferentially absorbed into astrocytes by the monocarboxylate transporter (MCT) [15,16]. Notably, the expression of MCT is increased in MS brains [17]. Therefore, we surmised that ^{11}C-acetate PET could be a useful diagnostic tool in combination with MRI, and we investigated the utility of ^{11}C-acetate PET for the diagnosis of MS and evaluated the astrocyte activity in the MS brain.

Materials and Methods

Subjects and clinical evaluation

Six patients with relapsing-remitting MS were evaluated. All patients were in the remission phase. Disability was assessed based

Table 1. Patient data and demographics.

	sex	age	type	therapy	EDSS score	Disease duration (y)	GM SUVt	WM SUVt	WM/GM ratio
MS 1	F	47	RR	IFNβ, MTX	7	10.3	1.0494	0.9415	0.8972
MS 2	F	45	RR	IFNβ	2	6.8	1.1069	1.0529	0.9512
MS 3	F	48	RR	IFNβ	1	5.7	1.0282	0.8874	0.8631
MS 4	F	53	RR	IFNβ	2.5	7.4	1.0837	0.9434	0.8705
MS 5	F	34	RR	-	4	3.3	0.9633	0.8244	0.8558
MS 6	F	49	RR	-	1	1.4	1.0336	0.9044	0.8750
HV 1	F	54					0.9149	0.7320	0.8001
HV 2	F	61					0.9671	0.8121	0.8397
HV 3	F	41					0.9518	0.7789	0.8183
HV 4	F	67					0.9341	0.7946	0.8507
HV 5	F	62					0.9449	0.8021	0.8489
HV 6	F	63					0.9758	0.8096	0.8297

MS = multiple sclerosis, HV = healthy volunteer, RR = relapsing-remitting multiple sclerosis, IFNβ = interferon beta treatment, MTX = Mitoxantrone, EDSS = Expanded Disability Status Scale, SUV = standardized uptake value.
doi:10.1371/journal.pone.0111598.t001

on the Expanded Disability Status Scale (EDSS) [18]. Six healthy volunteers (HV) served as normal controls (Table 1). This study was approved by the Ethics Committee of Osaka University Hospital, and written informed consent was obtained from each participant.

MRI

MRI was performed using a GE SIGNA HDxt 3.0-T or a Phillips Achieva 3.0-T scanner. Three-dimensional (3D) structural MRI was performed for each subject using a T1-weighted spoiled gradient recalled (SPGR) sequence (axial plane; slice thickness, 0.90/0.95 mm; matrix size, 512×512; in-plane resolution, 0.47×0.47 mm; TR, 2.144 to 2.192/2.477 to 2.53 ms; TE, 6.908 to 7.108/6.000; flip angle, 18°/15°) and T2-weighted two-dimensional fast spin echo sequences (axial plane; FOV 250 mm; matrix size, 512×512; slice thickness, 5 mm; interslice gap, 1 to 1.5 mm; TE, 89/80 ms; TR, 4500/3000 ms).

PET

PET was performed using a SET-3000 GCT/X scanner (Shimadzu Corp., Kyoto, Japan). ^{11}C-acetate was synthesized by carbonation of Grignard reagent followed by acid hydrolysis. ^{11}C-carbon dioxide reacted with methylmagnesium bromide followed by hydrolysis with hydrochloric acid to yield ^{11}C acetic acid [19]. The radio chemical purity was greater than 98%. A total of 370 MBq of the tracer was administered intravenously, and a 20-min emission acquisition was initiated 20 min later. PET images were obtained in a 3-D mode. The images were reconstructed using a filtered-back projection method after 3D Gaussian smoothing with a 6-mm full width at half maximum (FWHM). Scatter correction was performed using a hybrid dual-energy window method combined with a convolution-subtraction method, and the true scatter-free component of the standard photopeak window was estimated sonographically. All PET images were reconstructed in 256×256×99 anisotropic voxels, with each voxel measuring 1×1×2.6 mm.

Data analysis

Whole brain VOI analysis. All procedures were performed using a personal computer (DELL Precision T7400; DELL Inc., Round Rock, TX, USA) running on Microsoft Windows 7 (Microsoft Corp., Redmond, WA, USA). The 3D T1-weighted MRI scan was re-sliced in the native space of each subject using a 1.0×1.0×1.0 mm voxel size. The results were first categorized as GM, WM, and CSF, then spatially normalized using the unified model [20] of Statistical Parametric Mapping (SPM) 8 (Wellcome Department of Imaging Neuroscience: http://www.fil.ion.ucl.ac.uk/spm/) according to the optimized voxel-based morphometry (VBM) protocol [21]. This generated both spatial normalization matrices and inverse spatial normalization matrices. The resulting normalized GM map was transformed into native space using an inverse spatial normalization matrix. To generate VOI for GM and/or WM, binary mask images for the GM and/or WM were created using the segmented images in the native space of each subject. The binary mask image boundary was set at 35% of the maximum GM or WM concentration as described in previous studies [22,23].

The ^{11}C-acetate PET images were co-registered with the resliced 3D T1-weighted MRI using the SPM8 registration function based on the mutual information. The co-registration precision was inspected with the "Check Registration" tool in SPM8. Then, the co-registered PET images were spatially transformed using normalization and/or inverse normalization matrices identical to those generated in the previously described

automatic segmentation process. The ^{11}C -acetate uptake in the GM and WM VOI was analyzed using the binary masks within the native space.

To minimize contamination from the spill-in effect of adjacent brain segments, the spill-in-free VOIs of GM and WM were generated by the VOI erosion process. First, the binary masks were blurred by convolution using the point spread function of the PET scanner (presumably a simple isotropic Gaussian kernel with a FWHM of 8 mm). The spill-in-free gray matter mask $\hat{G}$ is expressed as follows:

$$\hat{G}=\{x \in G | \tilde{W}(x)<0.1\},$$

where x is a voxel, G is the gray matter binary mask, and $\tilde{W}(x)$ is the blurred image of the white matter binary mask (i.e. spill-in fraction from the white matter to the voxel x). The spill-in-free white matter mask was also constructed as described above. Spill-in from CSF was assumed as zero. VOI analysis for ^{11}C-acetate uptake using spill-in-free GM and WM masks was also performed (Figure S1).

The relative standardized uptake value (SUVt) served as the uptake indicator for analysis; the regional standardized uptake value (SUV) was divided by the mean SUV within the bilateral thalami of each subject. The Mann–Whitney U test was performed to determine significance of ^{11}C -acetate SUVt differences between MS and HV. The significance level was designated at $p<0.05$.

Voxel-based statistical analysis. Voxel-based whole brain SUVt in the MS and HV groups was compared using Statistical Parametric Mapping (SPM) 8 (Wellcome Department of Imaging Neuroscience). The spatially normalized PET images were smoothed using a 12-mm FWHM isotropic Gaussian kernel, which conditions the residuals to conform more closely to the Gaussian random field model underlying the statistical adjustment of the p values. The SPM statistical model used voxel-by-voxel "two-sample T-test with covariates," which designated age as a nuisance variable in order to detect voxels showing a significant age-adjusted SUVt difference between the MS and HV groups.

11C-acetate uptake and the MR images correlation assessment. The T2 and T1 black hole lesions were independently recorded visually by three observers. T1 black holes were defined as visible hypointense regions on the T1- weighted images coincident with a high signal intense region on the T2-weighted images. Each MRI mask image was divided into its hemispheres to create the hemispheric VOIs. Pearson product moment correlation analyses were performed to assess the association between the number of MRI lesions, and the SUV of ^{11}C-acetate was accessed from the hemispheric VOIs of the GM and WM. Statistical significance was designated at $p<0.05$.

Statistical analysis

The data in Fig 1 and Table S1 were analyzed using the Mann–Whitney U test. ANCOVA was used to assess the differences between age-adjusted groups illustrated in Fig 2B–G, and Pearson product moment correlation analyses were performed for data in Fig 3, SPSS 14.J was used for statistical analysis.

Results

VOI analysis of the ^{11}C-acetate SUV revealed that the mean SUV was higher in the MS patients than in the HV in all regions assessed (Fig 1A). To evaluate the regional distribution of ^{11}C-acetate uptake independent of physiologic variation in the whole brain, we calculated the relative uptake value (SUVt), which is the regional SUV divided by the mean SUV within the bilateral thalami of each participant (Fig 1B). The thalamus served as the reference region because it is rarely involved in MS pathology [24], and the SUV difference between the thalamus of HV and MS patients was the least among brain regions, as shown in Fig 1A. Each regional SUVt in the MS patients were increased particularly in the parietal, occipital, and insula regions.

Spatially normalized group mean images of ^{11}C-acetate SUVt automatically segmented based on MRI showed increased uptake in both WM and GM in MS patients (Fig 2A). The SUVt of MS patients was significantly higher than that of HV in both WM ($p=0.002$) and GM ($p=0.001$). In addition, all six MS patients had a significantly higher WM/GM SUV ratio than the six HV ($p=0.009$) (Fig 2B–D). This trend was consistently observed even after accommodating spill-in effect from adjacent brain segments (Fig 2E–G). Collectively, the ^{11}C-acetate uptake significantly increased in both the WM and GM of MS patients, and this increase was more predominant in WM. The whole brain SPM analysis revealed a significant increase in SUVt of voxel cluster in MS patients compared to HV, primarily in the subcortical frontal, parietal, and occipital regions; no voxels showed a significantly lower SUVt in MS patients compared to HV (Fig 2H).

The voxel-based t-statistic for the WM tracts showed a significantly increased mean T-score, predominantly in the superior longitudinal fasciculus, posterior thalamic radiation, and sagittal stratum, with the highest local maximum T-score in the corpus callosum (Table S2).

We then assessed potential correlation between ^{11}C-acetate SUV and MRI brain lesions. The mean SUV in WM was significantly correlated to the number of T1 black holes ($R^2=0.5059$, $p=0.009$) and T2 lesions ($R^2=0.4594$, $p=0.015$) (Fig 3A, B). The mean SUV in GM also correlated to the number of T1 black holes ($R^2=0.4088$, $p=0.025$) and T2 lesions ($R^2=0.3952$, $p=0.029$) (Fig 3C, D). The correlation to the EDSS score and disease duration did not reach statistical significance.

Discussion

There have been few studies imaging astrocytes in vivo using ^{11}C-acetate PET. In MS, astrocyte proliferation [25] and formation of scars composing a dense network of hypertrophic cells are characteristics of the MS histopathology [8]. An increased MCT expression in astrocytes within MS lesions was recently shown by immunohistochemical analysis [17], which suggest an increase in astrocyte metabolism. However, latent autoantibody-mediated astrocyte damage [26] supposedly decreases the metabolic activity, and therefore, the metabolic activity of astrocytes in MS brains remains undetermined. In this study, we observed a significantly increased brain uptake of the radioligand ^{11}C-acetate in MS patients. Our study revealed for the first time that astrocytes are generally activated in MS brains based on the acetate metabolism.

Representative studies showed that a higher value in the kinetic parameter, which indicates the washout level of ^{11}C-acetate, reflects the astrocyte reactivity in normal rats and healthy humans [27]. In MS, however, compared to HV, the pathologic changes in the severity of ^{11}C-acetate accumulation may be much more prominent than the changes related to physiologic activation in healthy humans. Therefore, a slight increase in the washout speed may be inapparent in the PET SUV in MS. Furthermore, because the perfusion in the normal appearing white matter decreased in MS [28], the increase in ^{11}C-acetate uptake by static PET may be underestimated due to a reduced CBF in MS.

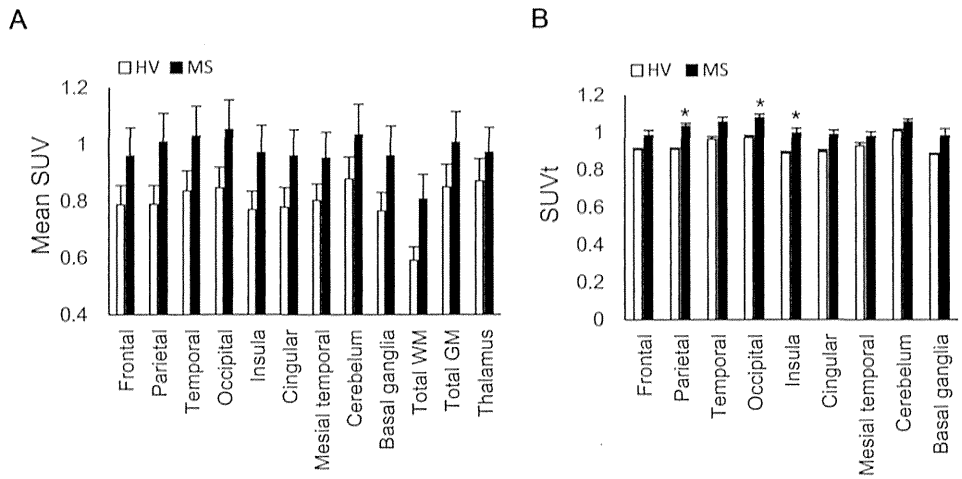

Figure 1. ^{11}C-acetate CNS biodistribution. (A)Mean standardized uptake value (SUV) of each lesion. (B) Relative SUV compared to that of the thalamus (SUVt). Data are expressed as the mean ± standard error of the mean (SEM) (n = 6). The Mann–Whitney *U* test showed a significant difference in the median between the HV and MS groups (*:p<0.0055 after Bonferroni correction). HV = healthy volunteers, MS = multiple sclerosis.
doi:10.1371/journal.pone.0111598.g001

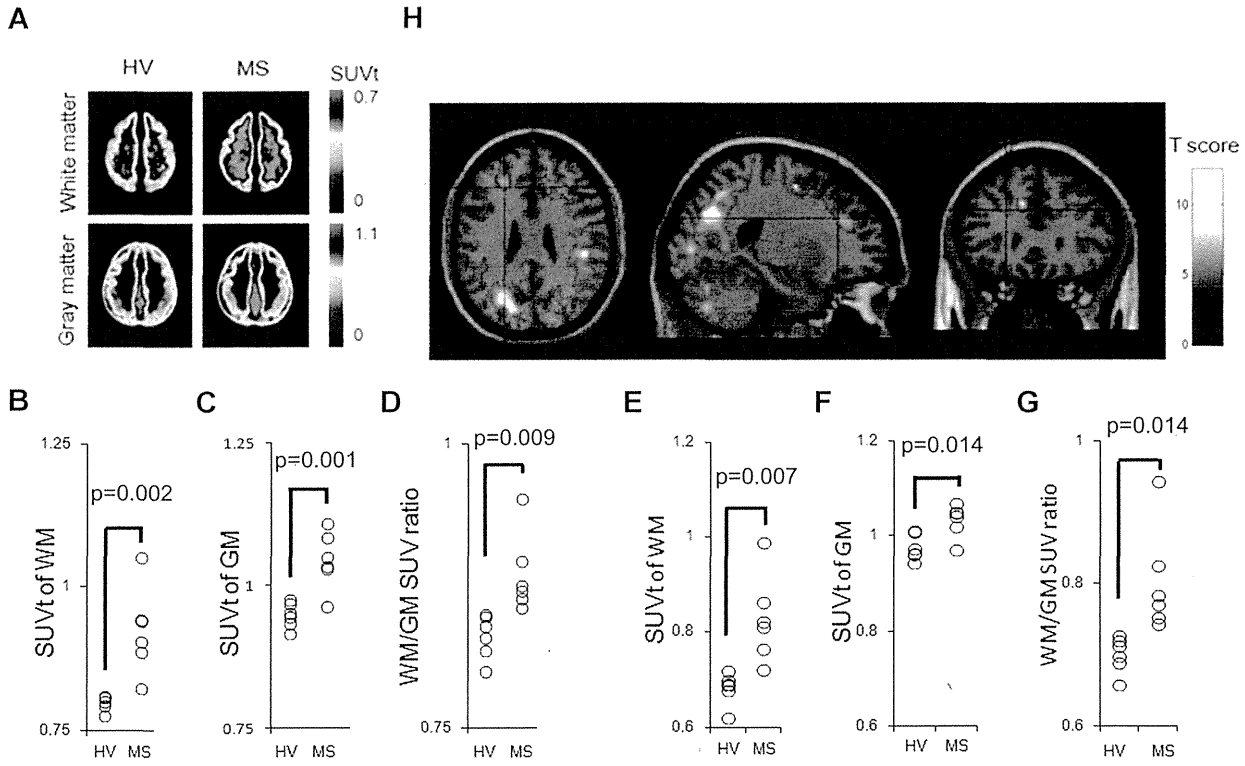

Figure 2. ^{11}C-acetate uptake distribution and quantification in MS patients. (A)Spatially normalized group mean images of ^{11}C-acetate SUVt automatically segmented based on MRI. VOI analysis summarizing the mean SUVt in WM (B) and GM (C), and the WM/GM SUV ratio (D) in the HV and MS groups. The identical analysis performed using spill-in-free VOIs are also shown (E–G). The p-value was calculated using the analysis of covariance to adjust the variance of age. (H) The SPM analysis result is overlaid onto the T1-weighted brain MRI template. Colored voxels indicate T-scores representing significantly increased ^{11}C-acetate uptake (SUVt) in patients with MS compared to HV patients. The spatially normalized PET images were smoothed for the analysis using a 12-mm FWHM isotropic Gaussian kernel. The significance thresholds are corrected for multiple comparisons at the cluster level with a p-value of 0.05 (family-wise error correction). SUV: standardized uptake value.
doi:10.1371/journal.pone.0111598.g002

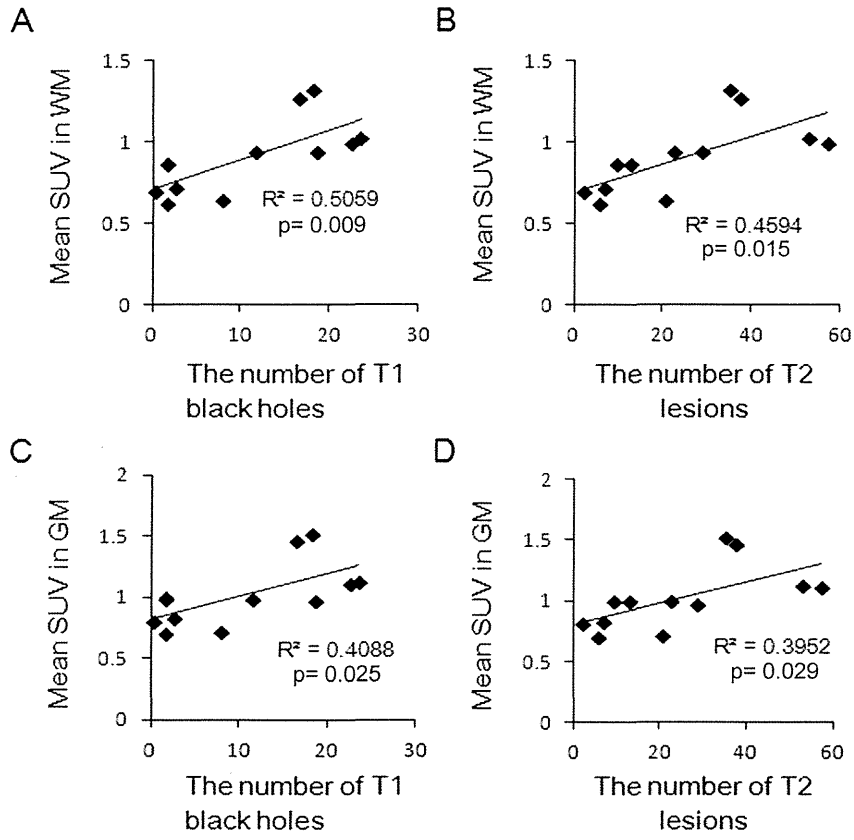

Figure 3. Correlation between ^{11}C-acetate SUV and the number of MRI lesions in patients with MS. Correlation between ^{11}C-acetate SUV in WM or GM and the number of T1 black holes (A, C) or T2 lesions (B, D) in each hemisphere of the six MS patients. SUV: standardized uptake value.
doi:10.1371/journal.pone.0111598.g003

The increased uptake was more pronounced in the WM, although a significant increase was observed in both the WM and GM. A significantly increased uptake was observed primarily within the subcortical WM on the voxel-based statistical analysis (Fig. 2H). On the voxel-based statistical analysis of the WM tracts, the distribution of the increased acetate uptake was similar to that in regions of axonal damage in DTI studies (Table S2). Recent voxel- and tract-based analyses in DTI studies revealed widespread damage to the subcortical WM, particularly in the sagittal stratum, corpus callosum, posterior thalamic radiation, and corona radiata [29]. These data suggested that the region-dependent increased acetate uptake was induced by the reactive astrocyte coexisting with heterogeneously dispersed MS lesions detected in DTI studies (Fig. 2H and Table S2). Although inflammatory WM demyelination detected by conventional MRI is a cardinal feature of MS, pathologic changes exist even in normal appearing WM and GM [30]. Astrocyte pathology precedes demyelination in an animal model [31]; astrocyte hypertrophy occurs at the leading edge of acute MS lesions, followed later by astrocytic scarring [8]. Thus, the altered astrocyte activation is presumably involved in MS pathophysiology [4,7,32]. Correlation between the radial diffusivity quantified by DTI and T1 black hole formation are recognized markers of axonal loss and tissue destruction [33,34]. In the present study, the strongest correlation was detected between the mean SUV in WM and the T1 black hole number, suggesting that the mean SUV may correlate with axonal damage. The mean SUV in GM also increased and correlated with the number of MRI lesions, suggesting cortical astrocyte involvement in MS pathology. Cortical involvement and subsequent cognitive decline occur in approximately half of MS patients [35]. However, little information exists on the pathophysiologic involvement of cortical astrocytes [36]. Normally, astrocytes supply lactate to neurons for oxidation [37], and metabolic dysfunction of neurons and glial cell activation likely occurs in the MS brain [25]. Moreover, astrocytes are associated with preclinical axonal damage in an animal model of MS [38]. These results suggest that the increased ^{11}C-acetate uptake within GM may reflect astrocyte-associated cortical damage in MS.

The present study has a few limitations. First, ^{11}C-acetate uptake in MS plaques was not assessed separately because most plaques were so small that a partial volume effect caused by the relatively low resolution of PET was inevitable. Second, the analysis was performed on static PET data instead of kinetic parameters. In the present study, the data acquired between 20 to 40 min after tracer administration were summed to build static uptake images because the time activity curve stabilized after 20 min (data not shown). Regional uptake distribution may be contaminated by the dispersion of radioactive metabolites. However, in our study, 1-^{11}C-acetate was used, and its dispersion of labeled metabolites was the smallest among the various types of acetate tracers [39,40]. In addition, because almost all the tracer was first absorbed through MCT-1 expressed within astrocytes according to their reactivity, the summed radioactivity is thought to reflect the first uptake of ^{11}C- acetate and its subsequent

metabolism by reactive astrocytes. Finally, because the mean age was higher in the control group than in the MS group, we used the ANCOVA to assess the differences among the age-adjusted SUVt. Although the mean age of MS patients was generally lower than that of the healthy volunteers, age did not significantly affect the increased uptake of ^{11}C-acetate in MS patients.

Conclusions

The present study suggests that the pathologic white matter changes in patients with MS can be detected by non-invasive static ^{11}C-acetate PET, which may be an effective MS diagnostic tool. Development of clinically applicable monocarbonic acid tracers labeled with longer half-life radioactive nuclides are needed, as are further studies enrolling more participants, including those in the early and relapse phases.

Supporting Information

Figure S1 Binary mask imaging parameters for VOI analysis. The scheme of VOI analysis is described. A: ^{11}C-acetate PET, B: 3D MRI, C: Co-registration, D: Spatial normalization to the MNI space, E/F: Segmented GM/WM map in the MNI space, G/H: GM/WM binarized mask in the original space of the subject, I/J: Eroded version of G/H for spill-in-free VOI analysis, K–N: GM/WM masks overlaid onto PET in the original space of the subject. MNI: montreal neurological institute. f: Transformation matrix for spatial normalization, f^{-1}: Inverse of the transformation.
(TIF)

Table S1 Relative ^{11}C-acetate biodistribution in the CNS. The mean SUVt of each lesion in the CNS was analyzed and for group comparison between HV and MS patients, the Mann–Whitney *U* test was performed.
(DOC)

Table S2 Regional T-scores from voxel-based statistical comparison in WM. Voxel-based statistical comparison in white matter tracts was performed. The positive T-scores indicate an increased ^{11}C-acetate uptake in the MS patients compared to the HV.
(DOC)

Text S1 Supplementary methods. Methods for "Voxel-based statistical analysis for WM tracts" are described with references.
(DOC)

Acknowledgments

We thank Dr. Hisashi Tanaka, Dr. Yoshiyuki Watanabe, Dr. Kayako Isohashi, Mr. Koichi Fujino, Mr. Yasukazu Kanai, Mr. Sadahiro Naka, and the staff of the Department of Nuclear Medicine and the Cyclotron staff of Osaka University Hospital for their technical support in performing the studies.

Author Contributions

Conceived and designed the experiments: YN HM JH. Performed the experiments: HK ES. Analyzed the data: KT HK TO TK TS. Wrote the paper: KT HK YN.

References

1. Compston A, Coles A (2002) Multiple sclerosis. Lancet 359: 1221–1231.
2. Sormani MP, Bruzzi P (2013) MRI lesions as a surrogate for relapses in multiple sclerosis: a meta-analysis of randomised trials. Lancet Neurol 12: 669–676.
3. Odenthal A, Coulthard C (2014) The Prognostic Utility of MRI in Clinically Isolated Syndrome: A Literature Review. AJNR Am J Neuroradiol.
4. Fernando KT, McLean MA, Chard DT, MacManus DG, Dalton CM, et al. (2004) Elevated white matter myo-inositol in clinically isolated syndromes suggestive of multiple sclerosis. Brain 127: 1361–1369.
5. Banati RB, Newcombe J, Gunn RN, Cagnin A, Turkheimer F, et al. (2000) The peripheral benzodiazepine binding site in the brain in multiple sclerosis: quantitative in vivo imaging of microglia as a measure of disease activity. Brain 123 (Pt 11): 2321–2337.
6. Politis M, Giannetti P, Su P, Turkheimer F, Keihaninejad S, et al. (2012) Increased PK11195 PET binding in the cortex of patients with MS correlates with disability. Neurology 79: 523–530.
7. Black JA, Newcombe J, Waxman SG (2010) Astrocytes within multiple sclerosis lesions upregulate sodium channel Nav1.5. Brain 133: 835–846.
8. Brosnan CF, Raine CS (2013) The astrocyte in multiple sclerosis revisited. Glia 61: 453–465.
9. Brown M, Marshall DR, Sobel BE, Bergmann SR (1987) Delineation of myocardial oxygen utilization with carbon-11-labeled acetate. Circulation 76: 687–696.
10. Oyama N, Okazawa H, Kusukawa N, Kaneda T, Miwa Y, et al. (2009) 11C-Acetate PET imaging for renal cell carcinoma. Eur J Nucl Med Mol Imaging 36: 422–427.
11. Ho CL, Yu SC, Yeung DW (2003) 11C-acetate PET imaging in hepatocellular carcinoma and other liver masses. J Nucl Med 44: 213–221.
12. Oyama N, Akino H, Kanamaru H, Suzuki Y, Muramoto S, et al. (2002) 11C-acetate PET imaging of prostate cancer. J Nucl Med 43: 181–186.
13. Lin C, Ho CL, Ng SH, Wang PN, Huang Y, et al. (2014) (11)C-acetate as a new biomarker for PET/CT in patients with multiple myeloma: initial staging and postinduction response assessment. Eur J Nucl Med Mol Imaging 41: 41–49.
14. Liu RS, Chang CP, Chu LS, Chu YK, Hsieh HJ, et al. (2006) PET imaging of brain astrocytoma with 1-11C-acetate. Eur J Nucl Med Mol Imaging 33: 420–427.
15. Waniewski RA, Martin DL (1998) Preferential utilization of acetate by astrocytes is attributable to transport. J Neurosci 18: 5225–5233.
16. Hosoi R, Okada M, Hatazawa J, Gee A, Inoue O (2004) Effect of astrocytic energy metabolism depressant on 14C-acetate uptake in intact rat brain. J Cereb Blood Flow Metab 24: 188–190.
17. Nijland PG, Michailidou I, Witte ME, Mizee MR, van der Pol SM, et al. (2014) Cellular distribution of glucose and monocarboxylate transporters in human brain white matter and multiple sclerosis lesions. Glia 62: 1125–1141.
18. Kurtzke JF (1983) Rating neurologic impairment in multiple sclerosis: an expanded disability status scale (EDSS). Neurology 33: 1444–1452.
19. Ishiwata K, Ishii S-I, Senda M (1995) Successive preparation of 11C labeled sodium acetate and/or sodium hexanoate. Applied Radiation and Isotopes 46: 1035–1037.
20. Ashburner J, Friston KJ (2005) Unified segmentation. Neuroimage 26: 839–851.
21. Good CD, Johnsrude IS, Ashburner J, Henson RN, Friston KJ, et al. (2001) A voxel-based morphometric study of ageing in 465 normal adult human brains. Neuroimage 14: 21–36.
22. Hosoi R, Matsuyama Y, Hirose S, Koyama Y, Matsuda T, et al. (2009) Characterization of (14)C-acetate uptake in cultured rat astrocytes. Brain Res 1253: 69–73.
23. Kato H, Shimosegawa E, Isohashi K, Kimura N, Kazui H, et al. (2012) Distribution of cortical benzodiazepine receptor binding in right-handed healthy humans: a voxel-based statistical analysis of iodine 123 iomazenil SPECT with partial volume correction. AJNR Am J Neuroradiol 33: 1458–1463.
24. Brownell B, Hughes JT (1962) The distribution of plaques in the cerebrum in multiple sclerosis. J Neurol Neurosurg Psychiatry 25: 315–320.
25. Chard DT, Griffin CM, McLean MA, Kapeller P, Kapoor R, et al. (2002) Brain metabolite changes in cortical grey and normal-appearing white matter in clinically early relapsing-remitting multiple sclerosis. Brain 125: 2342–2352.
26. Srivastava R, Aslam M, Kalluri SR, Schirmer L, Buck D, et al. (2012) Potassium channel KIR4.1 as an immune target in multiple sclerosis. N Engl J Med 367: 115–123.
27. Wyss MT, Weber B, Treyer V, Heer S, Pellerin L, et al. (2009) Stimulation-induced increases of astrocytic oxidative metabolism in rats and humans investigated with 1-11C-acetate. J Cereb Blood Flow Metab 29: 44–56.
28. De Keyser J, Steen C, Mostert JP, Koch MW (2008) Hypoperfusion of the cerebral white matter in multiple sclerosis: possible mechanisms and pathophysiological significance. J Cereb Blood Flow Metab 28: 1645–1651.
29. Dineen RA, Vilisaar J, Hlinka J, Bradshaw CM, Morgan PS, et al. (2009) Disconnection as a mechanism for cognitive dysfunction in multiple sclerosis. Brain 132: 239–249.
30. Bjartmar C, Kinkel RP, Kidd G, Rudick RA, Trapp BD (2001) Axonal loss in normal-appearing white matter in a patient with acute MS. Neurology 57: 1248–1252.
31. Sharma R, Fischer MT, Bauer J, Felts PA, Smith KJ, et al. (2010) Inflammation induced by innate immunity in the central nervous system leads to primary